

# Brown dwarf census with the Dark Energy Survey year 3 data and the thin disc scale height of early L types

A. Carnero Rosell<sup>1,2,3\*</sup>, B. Santiago<sup>2,4</sup>, M. dal Ponte<sup>4</sup>, B. Burningham<sup>5</sup>,  
 L. N. da Costa<sup>2,3</sup>, D. J. James<sup>6,7</sup>, J. L. Marshall<sup>8</sup>, R. G. McMahon<sup>9,10</sup>, K. Bechtol<sup>11,12</sup>,  
 L. De Paris<sup>4</sup>, T. Li<sup>13,14</sup>, A. Pieres<sup>2,3</sup>, J. García-Bellido<sup>15</sup>, T. M. C. Abbott<sup>16</sup>, J. Annis<sup>13</sup>,  
 S. Avila<sup>15</sup>, G. M. Bernstein<sup>17</sup>, D. Brooks<sup>18</sup>, D. L. Burke<sup>19,20</sup>, M. Carrasco Kind<sup>21,22</sup>,  
 J. Carretero<sup>23</sup>, J. De Vicente<sup>1</sup>, A. Drlica-Wagner<sup>16,14</sup>, P. Fosalba<sup>24,25</sup>, J. Frieman<sup>13,14</sup>,  
 E. Gaztanaga<sup>24,25</sup>, R. A. Gruendl<sup>21,22</sup>, J. Gschwend<sup>2,3</sup>, G. Gutierrez<sup>13</sup>, D.  
 L. Hollowood<sup>26</sup>, M. A. G. Maia<sup>2,3</sup>, F. Menanteau<sup>21,22</sup>, R. Miquel<sup>23,27</sup>, A. A. Plazas<sup>28</sup>,  
 A. Roodman<sup>19,20</sup>, E. Sanchez<sup>1</sup>, V. Scarpine<sup>13</sup>, R. Schindler<sup>20</sup>, S. Serrano<sup>24,25</sup>,  
 I. Sevilla-Noarbe<sup>1</sup>, M. Smith<sup>29</sup>, F. Sobreira<sup>2,30</sup>, M. Soares-Santos<sup>31</sup>, E. Suchyta<sup>32</sup>,  
 M. E. C. Swanson<sup>22</sup>, G. Tarle<sup>33</sup>, V. Vikram<sup>34</sup> and A. R. Walker<sup>16</sup> (DES Collaboration)

*Affiliations are listed at the end of the paper*

Accepted 2019 August 28. Received 2019 July 12; in original form 2019 March 26

## ABSTRACT

In this paper we present a catalogue of 11 745 brown dwarfs with spectral types ranging from L0 to T9, photometrically classified using data from the Dark Energy Survey (DES) year 3 release matched to the Vista Hemisphere Survey (VHS) DR3 and Wide-field Infrared Survey Explorer (WISE) data, covering  $\approx 2400$  deg<sup>2</sup> up to  $i_{AB} = 22$ . The classification method follows the same phototype method previously applied to SDSS-UKIDSS-WISE data. The most significant difference comes from the use of DES data instead of SDSS, which allow us to classify almost an order of magnitude more brown dwarfs than any previous search and reaching distances beyond 400 pc for the earliest types. Next, we also present and validate the *GalmodBD* simulation, which produces brown dwarf number counts as a function of structural parameters with realistic photometric properties of a given survey. We use this simulation to estimate the completeness and purity of our photometric LT catalogue down to  $i_{AB} = 22$ , as well as to compare to the observed number of LT types. We put constraints on the thin disc scale height for the early L (L0–L3) population to be around 450 pc, in agreement with previous findings. For completeness, we also publish in a separate table a catalogue of 20 863 M dwarfs that passed our colour cut with spectral types greater than M6. Both the LT and the late M catalogues are found at DES release page <https://des.ncsa.illinois.edu/releases/other/y3-mlt>.

**Key words:** techniques: photometric – catalogues – surveys – brown dwarfs – Galaxy: fundamental parameters – infrared: stars.

## 1 INTRODUCTION

Ultra-cool dwarfs are mostly sub-stellar objects (brown dwarfs, BDs) with very cool ( $T_{\text{eff}} < 2300$  K) atmospheres with spectral types later than M7, including the L, T, and Y sequences. Their spectra are typified by the effects of clouds and deep molecular absorption bands. In L dwarfs ( $2200 \text{ K} \gtrsim T_{\text{eff}} \gtrsim 1400 \text{ K}$ ) clouds

block radiation from emerging from deep in the atmosphere in the opacity windows between molecular absorption bands, narrowing the pressure range of the observed photosphere, and redistributing flux to longer wavelengths giving these objects red near-infrared colours. The transition to the T sequence (LT transition,  $T_{\text{eff}} \sim 1200\text{--}1400$  K) is driven by the disappearance of clouds from the near-infrared photosphere, leading to relatively bluer colours. This is accompanied by the transition from CO (L dwarfs) to CH<sub>4</sub> (T dwarfs) dominated carbon chemistry. At cooler temperatures ( $T_{\text{eff}} < 500$  K), the development of the Y dwarf sequence is thought to be

\* E-mail: [aurelio.crosell@gmail.com](mailto:aurelio.crosell@gmail.com)

driven by the emergence of clouds due to sulphide and chloride condensates, as well as water ice (e.g. Leggett et al. 2013, 2015; Skemer et al. 2016).

BDs never achieve sufficient core temperatures to maintain main-sequence hydrogen fusion. Instead, they evolve from relatively warm temperatures at young ages to ever cooler temperatures with increasing age as they radiate the heat generated by their formation. As a result, the late M and early L dwarf regime includes both young, high-mass, BDs and the lowest mass stars. The latter can take several hundred million years to reach the main sequence. Objects with late L, T, and Y spectral types are exclusively substellar. In this work, we focus on L and T dwarfs, and for brevity refer to this group as BDs.

BDs have very low luminosity, especially the older or lower mass ones. Their mass function, star formation history (SFH), and spatial distribution are still poorly constrained, and the evolutionary models still lack details, especially the lowest masses and old ages. They are supported at their cores by degenerate electron pressure and, because the degeneracy determines the core density (instead of the Coulomb repulsion), more massive BDs have smaller radii. BDs are actually partially degenerate, in the sense that while in their atmospheres reign thermal pressure, somewhere in their interior there must be a transition from degenerate electron to thermal pressure.

The current census covers an age range from a few million years (Liu et al. 2013; Gagné et al. 2017) to  $>10$  Gyr halo members (Burgasser et al. 2003; Zhang et al. 2017), and spans the entire mass interval between planetary and stellar masses. The diverse range of properties that these objects display reflects the continual luminosity and temperature evolution of these partially degenerate objects. As a numerous and very long-lived component of our Galaxy, these continually evolving objects could be used to infer structural components of the Milky Way (MW), and tracing the low-mass extreme of star formation over cosmic time-scales. However, studies of L dwarfs have typically been restricted to the nearest 100 pc, while T dwarfs are only known to distances of a few tens of parsecs.

The era of digital wide-field imaging surveys has allowed the study of BDs to blossom, with thousands now known in the solar neighbourhood. But this collection is heterogeneous and very shallow and therefore, not suitable for large-scale statistical analysis of their properties. The new generation of deep and wide surveys [DES (Dark Energy Survey Collaboration 2016), VHS (McMahon et al. 2013), UKIDSS (Lawrence et al. 2007), LSST (Abell et al. 2009), Hyper Suprime Camera (HSC; Miyazaki et al. 2018)] offer the opportunity to place the BD population in their Galactic context, echoing the transition that occurred for M dwarfs with the advent of the Sloan Digital Sky Survey (SDSS; Bochanski et al. 2007; West et al. 2011). These surveys should be able to create homogeneous samples of BDs to sufficient distance to be suitable for various applications, such as kinematics studies (Faherty et al. 2009, 2012; Schmidt et al. 2010; Smith et al. 2014), the frequency of binary systems in the LT population (Burgasser et al. 2006a; Burgasser 2007; Luhman 2012), benchmark systems (Pinfield et al. 2006; Burningham et al. 2013; Marocco et al. 2017), the search for rare or unusual objects (Burgasser et al. 2003; Folkes et al. 2007;Looper et al. 2008; Skrzypek et al. 2016), and the study of Galactic parameters (Ryan et al. 2005; Jurić et al. 2008; Sorahana et al. 2018). In this latter case, we will also need simulations to confront observed samples. Realistic simulations will benefit from improved spectral type luminosity and spectral type local density relations in the solar neighbourhood.

The UKIRT Infrared Deep Sky Survey (UKIDSS; Lawrence et al. 2007) imaged  $4000 \text{ deg}^2$  in the  $Y, J, H, K$  filter passbands, and provided discovery images for over 200 T dwarfs, making

it one of the principal contributors to the current sample of LT dwarfs, particularly at fainter magnitudes (e.g. Burningham et al. 2010; Burningham et al. 2013; Burningham 2018). Experience gained through the exploitation of UKIDSS has demonstrated that significant amounts of 8m-class telescope time are required to spectroscopically classify samples of 10s to 100s of LT dwarfs within 100 pc. For example, total observation times of 40–60 min were needed to obtain low-resolution spectra of  $J \sim 18.5$  targets at a signal-to-noise ratio (SNR) = 20, necessary for spectral classification (Burningham et al. 2013). Obtaining homogeneous samples to the full depth available in the new generation of surveys is thus only feasible today through photometric classification. Such an approach was demonstrated in Skrzypek et al. (2015, 2016), where they obtained a sample of more than 1000 LT dwarfs, independent of spectroscopic follow-up, using  $i, z, Y, J, H, K_s, W1, W2$  from  $\text{SDSS} \cap \text{UKIDSS} \cap \text{WISE}$ .

A summary of surveys that attempted to select BDs candidates photometrically can be found in Table 1. We identify two approaches: one based on a colour selection in optical bands and another with colour selection in the near-infrared. In the first case, a common practice is to apply a cut on  $(i - z)$ . For example, Schmidt et al. (2010) apply a cut at  $(i - z)_{\text{SDSS}} > 1.4$ , while Chiu et al. (2006) cut at  $(i - z)_{\text{SDSS}} > 2.2$  to select T types. This latter cut would be interesting to study the transition between L and T types, but not for a complete sample of L types. In any case, since the  $i, z$  bands in DES are not precisely the same as in SDSS, we expect changes in our nominal colour cuts.

When infrared bands are available, it is common to make the selection on  $J$  band. For example, Skrzypek et al. (2016) apply a cut on Vega magnitudes  $(Y - J)_{\text{UKIDSS, Vega}} > 0.8$ , which, in our case, would translate into  $(Y_{\text{AB}} - J_{\text{Vega}})_{\text{UKIDSS}} > 1.4$ . Burningham et al. (2013) search for T types, applying a cut at  $z_{\text{AB}} - J_{\text{Vega}} > 2.5$ . Again, the UKIDSS filters are not exactly the same as DES or VHS, so we expect these cuts to change when applied to our data.

In this paper, we follow the phototype methodology of Skrzypek et al. (2015) to find and classify L and T dwarfs in the  $\text{DES} \cap \text{VHS} \cap \text{AllWISE}$  system. (The AllWISE programme was built by combining data from the WISE cryogenic and NEOWISE post cryogenic phases.) We can go to greater distances due to the increased depth in the DES optical bands  $i, z$  in comparison with SDSS while maintaining high completeness in the infrared bands, needed for a precise photometric classification. In fact, the optical bands can drive the selection of L dwarfs, as demonstrated here, improving upon previous photometric BDs searches. In the case of T dwarfs, the infrared bands are the limiting ones, and therefore, our sample will have a similar efficiency in that spectral regime in comparison with previous surveys.

The methodology is based on three steps: first, a photometric selection in colour space  $(i - z), (z - Y), (Y - J)$  is done; secondly, a spectral classification is performed by comparing observed colours in  $i, z, Y, J, H, K_s, W1, W2$  to a set of colour templates for various spectral types, ranging from M1 to T9. These templates are calibrated using a sample of spectroscopically confirmed ultra-cool dwarfs (MLT). Finally, we remove possible extragalactic contamination with the use of a galaxy template fitting code, in particular, we use LEPHARE photo- $z$  code<sup>1</sup> (Arnouts et al. 1999; Ilbert et al. 2006).

After completion of a homogeneous sample of LT dwarfs, we proceed to measure the thin discscale height ( $h_{z, \text{thin}}$ ). Unfortunately,

<sup>1</sup><http://www.cfht.hawaii.edu/arnouts/LEPHARE/lephare.html>

**Table 1.** Summary of the major photometric BD census so far. In the third column we show the colour selection in its original systems, according to the surveys used (indicated in the first column). For comparison, we also show the selection used in this paper, where we classify more than 10 000 BDs up to  $z_{AB} = 22$ .

Reference (Surveys)	Area (deg <sup>2</sup> )	Selection	Spectral types	Number
Chiu et al. (2006) (SDSS)	3526	$(i - z)_{AB} > 2.2,$ $z_{AB} < 20.4$	LT	73
Schmidt et al. (2010) (SDSS, 2MASS)	11 000	$(i - z)_{AB} > 1.4$	L	484
Albert et al. (2011) (CFHT)	780	$(i - z)_{AB} > 2.5$	T	37
Kirkpatrick et al. (2011) (WISE)	All sky	T5: $(W1 - W2)_{Vega} > 1.5,$ $(W2 - W3)_{Vega} < 3$ L: $(W1 - W2)_{Vega} > 0$	LT	103
Lodieu et al. (2012) (VHS, WISE)	675	$(W1 - W2)_{Vega} > 1.4,$ $(J - W2)_{Vega} > 1.9$	T	13
Day-Jones et al. (2013) (UKIDSS)	500	$J_{Vega} < 18.1$	LT	63
Burningham et al. (2013) (UKIDSS)	2000	$(z_{AB} - J_{Vega}) > 2.5,$ $J_{Vega} < 18.8$	T	76
Skrzypek, Warren & Faherty (2016) (SDSS, UKIDSS, WISE)	3070	$(Y - J)_{Vega} > 0.8,$ $J_{Vega} < 17.5$	LT	1361
Sorahana, Nakajima & Matsuoka (2018) (HSC)	130	$1 < (i - z)_{AB} < 2.0,$ $0.75 < (z - Y)_{AB} < 1.0,$ $z_{AB} < 24$	L	3665
This paper (2019) (DES, VHS, WISE)	2400	$(i - z)_{AB} > 1.2,$ $(z - Y)_{AB} > 0.15,$ $(Y_{AB} - J_{Vega}) >$ $1.6,$ $z_{AB} < 22$	LT	11 745

**Table 2.** Information about the photometric passbands from DES Y3, VHS DR3, and AllWISE. Columns are the survey acronym, the filter name, the effective wavelength, and the magnitude limit at  $5\sigma$  in AB.

Survey	Filter	$\lambda_c$ ( $\mu\text{m}$ )	$m_{5\sigma}$ (AB)
DES	<i>i</i>	0.775	23.75
DES	<i>z</i>	0.925	23.05
DES	<i>Y</i>	1.0	20.75
VHS	<i>J</i>	1.25	21.2
VHS	<i>H</i>	1.65	19.85
VHS	<i>K<sub>s</sub></i>	2.15	20.4
AllWISE	<i>W1</i>	3.4	19.80
AllWISE	<i>W2</i>	4.6	19.04

current simulations present many inconsistencies with observations and are not trustworthy. Therefore, we also introduce a new simulation that computes expected number counts of LT dwarfs and creates synthetic samples following the properties of a given survey. We have called it *GalmodBD*. Finally, we can compare the output of the simulation for different formation scenarios, to the number of BDs found in the sample footprint, placing constraints on  $h_{z,\text{thin}}$  and other fundamental parameters.

In Section 2, we describe the data used in this paper ( $\text{DES} \cap \text{VHS} \cap \text{AllWISE}$ ) and how these samples were matched and used through the analysis. In Section 3, we detail the samples we have used to define our colour selection as well as to create the colour templates that will feed the classification and the *GalmodBD* simulation.

In Section 4, we show the colour-based target selection scheme we have defined and how it compares with the previous analysis, in particular to Skrzypek et al. (2015). In Section 5, we explain our classification methodology and how we apply it to the DES data in Section 6. In Section 7, we detail the public catalogue. In Sections 8 and 9 we introduce the *GalmodBD* simulation and how we tune it to our data in Section 10. In Section 11 we present results of running the simulation. In Section 12 we use the *GalmodBD* to study the completeness of our photometric selection and other systematics applying to the number of BDs detected. Finally, in Section 13 we compare results from the *GalmodBD* simulation to our data, placing constraints on the thin disc scale height of L types.

With the exception of Table 2, where we give the magnitude limit in the AB system for all bands, we will use throughout the paper the photometric bands *i*, *z*, *Y* from DES in AB magnitudes, *J*, *H*, *K<sub>s</sub>* from VHS in Vega and *W1*, *W2* from AllWISE in Vega. The use of Vega or AB normalization is not important since it is only a constant factor when calculating colours.

## 2 THE DATA

In this section, we present the three photometric data sets used in this analysis: the Dark Energy Survey (DES), with five filters covering from 0.38 to 1  $\mu\text{m}$  (from which we use *i*, *z*, *Y*), VHS, with three filters covering from 1.2 to 2.2  $\mu\text{m}$  and AllWISE *W1* and *W2*, at 3.4 and 4.6  $\mu\text{m}$ . Finally, in Section 2.4 we detail the catalogue matching process and quality cuts.

### 2.1 The Dark Energy Survey (DES)

DES is a wide-field optical survey in the *g*, *r*, *i*, *z*, *Y* bands, covering from 3800  $\text{\AA}$  to  $\sim 1 \mu\text{m}$ . The footprint was designed to avoid

extinction contamination from the Milky Way as much as possible, therefore pointing mostly towards intermediate and high Galactic latitudes. The observational campaign ended on 2019 January 9. The final DES data comprises 758 nights of observations over 6 yr (from 2013 to 2019).

In this paper we use DES year 3 (Y3) data, an augmented version of the Data Release 1 (The DR1; Dark Energy Survey Collaboration 2018)<sup>2</sup> which contains all the observations from 2013 to 2016. DES DR1 covers the nominal 5000 deg<sup>2</sup> survey region. The median coadded catalogue depth for a 1.95 arcsec diameter aperture at S/N = 10 is  $i \sim 23.44$ ,  $z \sim 22.69$ , and  $Y \sim 21.44$ . DR1 catalogue is based on coaddition of multiple single epochs (Morganson et al. 2018) using SEXTRACTOR (Bertin & Arnouts 1996). The DES Data Management (DESDM) system also computes morphological and photometric quantities using the ‘Single Object Fitting’ pipeline (SOF), based on the NGMIX<sup>3</sup> code, which is a simplified version of the MOF pipeline as described in Drlica-Wagner et al. (2018). The SOF catalogue was only calculated in  $g$ ,  $r$ ,  $i$ ,  $z$ , but not in  $Y$ , therefore we use SEXTRACTOR  $Y$  measurement from DR1 data. All magnitudes have been corrected by new zero-point values produced by the collaboration, improving over those currently published in the DR1 release.

Information about the mean wavelength of each passband and magnitude limit at  $5\sigma$  (defined as the mode of the magnitude distribution, as cited above, for a catalogue with S/N >  $5\sigma$ ) is given in Table 2. In Fig. 1 we show the DES footprint with coverage in  $i$ ,  $z$ ,  $Y$ . It has an area = 5019 deg<sup>2</sup> and all coloured areas represent the DES footprint.

To ensure high completeness in the  $i$  band and infrared bands with sufficient quality, we impose a magnitude limit cut of  $z < 22$  with a detection of  $5\sigma$  at least in the  $z$  and  $Y$  magnitudes. To avoid corrupted values due to image artefacts or reduction problems, we also apply the following cuts: SEXTRACTOR\_FLAGS\_Z, Y = 0: ensures no reduction problems in the  $z$  and  $Y$  bands. IMAPLANS\_ISO\_i, z, Y = 0: ensures the object has not been affected by spurious events in the images in  $i$ ,  $z$ ,  $Y$  bands.

## 2.2 VISTA Hemisphere Survey (VHS)

The VISTA Hemisphere Survey (VHS; McMahon et al. 2013) is an infrared photometric survey aiming to observe 18 000 deg<sup>2</sup> in the Southern hemisphere, with full overlap with DES in two wavebands,  $J$  and  $K_s$ , to a depth  $J_{AB} \sim 21.2$ ,  $K_{s,AB} \sim 20.4$  at  $5\sigma$  for point sources ( $J_{Vega} \sim 20.3$ ,  $K_{s,Vega} \sim 18.6$ , respectively) and partial coverage in  $H$  band, with depth  $H_{AB} \sim 19.85$  at  $5\sigma$  ( $H_{Vega} \sim 18.5$ ). The VHS uses the 4m VISTA telescope at ESO Cerro Paranal Observatory in Chile with the VIRCAM camera (Dalton et al. 2006). The data were downloaded by the DESDM system from the ESO Science Archive Facility (Cross et al. 2012) and the VISTA Science Archive.<sup>4</sup>

The VHS DR3 covers 8000 deg<sup>2</sup> in  $J$ ,  $K_s$  of observations from the year 2009 to 2013, from which a smaller region overlaps with DES, as shown in brown in Fig. 1. The coverage area in common with DES is 2374 deg<sup>2</sup> for the  $J$ ,  $K_s$  filters, whereas addition of the  $H$  band reduces this to 1331 deg<sup>2</sup> (shown as light brown in Fig. 1).

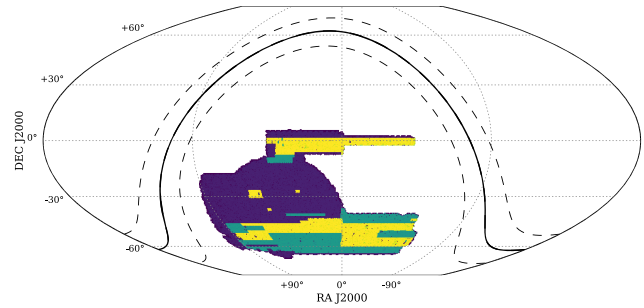


**Figure 1.** In purple, the footprint of DES Y3 data considering the intersection of  $i$ ,  $z$ ,  $Y$  bands in equatorial coordinates. The effective area for this region is 5019 deg<sup>2</sup>. In green and yellow, we show the overlap between DES and VHS, covering 2374 deg<sup>2</sup> with  $J$ ,  $K_s$ . The yellow region is the overlap with the three VHS bands  $J$ ,  $H$ ,  $K_s$  and it has an area of 1331 deg<sup>2</sup>. The Milky Way plane is depicted by the black line with a thickness of 20 deg.

In this paper, we use only sources defined as primary in the VHS data. We also impose  $5\sigma$  detection in  $J$ ; whenever  $H$ ,  $K_s$  are available, we use them for the spectral classification (see Section 5).

We use `apermag3` as the standard VHS magnitude, in the Vega system, defined as the magnitude for a fixed aperture of 2 arcsec. VHS aperture magnitudes are already aperture corrected. In Table 2 we show the summary of the filters and magnitude limits for VHS. VHS magnitude limits are in AB, even though we work in Vega throughout the paper. We use the transformation given by the VHS collaboration:<sup>5</sup>  $J_{AB} = J_{Vega} + 0.916$ ,  $H_{AB} = H_{Vega} + 1.366$ ,  $K_{s,AB} = K_{s,Vega} + 1.827$ .

## 2.3 ALLWISE

We also use AllWISE<sup>6</sup> data, a full-sky infrared survey in 3.4, 4.6, 12, and 22  $\mu$ m, corresponding to W1, W2, W3, W4, respectively. AllWISE data products are generated using the imaging data collected and processed as part of the original WISE (Wright et al. 2010) and NEOWISE (Mainzer et al. 2011) programmes.

Because LT colours tend to saturate for longer wavelengths, we will make use only of W1 and W2. The AllWISE catalogue is >95 per cent complete for sources with W1 < 17.1 and W2 < 15.7 (Vega).

In Table 2 we also show the properties of the AllWISE filters and magnitude limits. Magnitudes are given in AB using the transformations given by the collaboration:<sup>7</sup>  $W1_{AB} = W1_{Vega} + 2.699$ ,  $W2_{AB} = W2_{Vega} + 3.339$ .

Since our primary LT selection criteria do not use W1 and W2 magnitudes, we do not demand the availability of magnitudes in these bands when selecting our candidate sample. In other words, if a source has no data from AllWISE, we still keep it and flag their W1 and W2 magnitudes as unavailable in the classification.

## 2.4 Combining DES, VHS, and AllWISE data

We first match DES to VHS with a matching radius of 2 arcsec, and with the resulting catalogue, we repeat the same process to match to the AllWISE catalogue, using DES coordinates. The astrometric offset between DES and VHS sources was estimated in Banerji et al.

<sup>2</sup><https://des.ncsa.illinois.edu/releases/dr1>

<sup>3</sup><https://github.com/esheldon/ngmix>

<sup>4</sup><http://horus.roe.ac.uk/vsa/coverage-maps.html>

<sup>5</sup><http://casu.ast.cam.ac.uk/surveys-projects/vista/technical/filter-set>

<sup>6</sup><http://wise2.ipac.caltech.edu/docs/release/allwise/>

<sup>7</sup>[http://wise2.ipac.caltech.edu/docs/release/allsky/expsup/sec4\\_4h.html](http://wise2.ipac.caltech.edu/docs/release/allsky/expsup/sec4_4h.html)



(2015), giving a standard deviation of 0.18 arcsec. For sources with significant proper motions, this matching radius may be too small. For instance, an object at 10 pc distance, moving at  $30 \text{ km s}^{-1}$  in tangential velocity, has a proper motion of  $0.6 \text{ arcsec yr}^{-1}$ . So, a matching radius of 2 arcsec will work except for the very nearby ( $\leq 6 \text{ pc}$ ) or high-velocity ( $> 50 \text{ km s}^{-1}$ ) cases, given a 2-yr baseline difference in the astrometry. In fact, high-velocity nearby BDs are interesting, since they may be halo BDs going through the solar neighbourhood. A small percentage of BDs will be missing from our catalogue due to this effect. In Section 12 we quantify this effect.

We use the  $\text{DES} \cap \text{VHS} \cap \text{AllWISE}$  sample (called target sample) to find BDs. Matching the three catalogues and removing sources that do not pass the DES quality cuts, we find 42 046 583 sources. Applying the cut in SNR greater than  $5\sigma$  in  $z$ ,  $Y$ ,  $J$  and selecting sources with  $z < 22$ , we find 27 249 118 sources in our  $2374 \text{ deg}^2$  footprint.

Seeing and other observational variations through the footprint in a heterogeneous sample such as this one, could bias the measured colours of the target sample. Fortunately, DES, VHS, and WISE magnitudes are calibrated considering these variations and therefore, we assume homogeneity in all passbands. Likewise, the intrinsic colour variation of the LT population should be much larger than the effect caused by zero-point variations through the footprint, if they exist, and therefore indistinct of their intrinsic uncertainty.

Also, we do not account for interstellar reddening. Our target sample is concentrated in the solar neighbourhood and therefore, applying any known extinction maps, like Schlegel, Finkbeiner & Davis (1998) or Schlafly & Finkbeiner (2011) maps, we would overestimate the reddening.

### 3 CALIBRATION SAMPLES

In this section, we present and characterize the calibration samples used to define our colour selection (Section 4) and to create the photometric templates (see Section 3.4) that will be used during the spectral classification step (Section 5) and to feed the *GalmodBD* simulation (Section 8). Quasars are only used as a reference in the first stage, while the M dwarfs and BDs are used both to select the colour space and to create the colour templates that will be used during the analysis.

The calibration samples are J. Gagné’s compilation of BDs, M dwarf sample from SDSS, and spectroscopically confirmed quasars from DES. It is important to note that all of them have spectroscopic confirmation.

Each calibration sample has been matched to the target sample. In all cases, we again use a matching radius of 2 arcsec to DES coordinates.

#### 3.1 Gagné’s sample of brown dwarfs

The Gagné compilation<sup>8</sup> contains a list of most of the spectroscopically confirmed BDs up to 2014, covering spectral types from late M to LT dwarfs. It consists of 1772 sources, covering most parts of the sky to distances less than 100 pc. The spectral classification in this sample is given by its optical classification anchored to the standard L dwarf scheme of Kirkpatrick et al. (1999) or by its near-infrared classification anchored to the scheme for T dwarfs from Burgasser et al. (2006b). Some of the BDs present in this sample have both classifications. In most cases, both estimations agree, but for a few

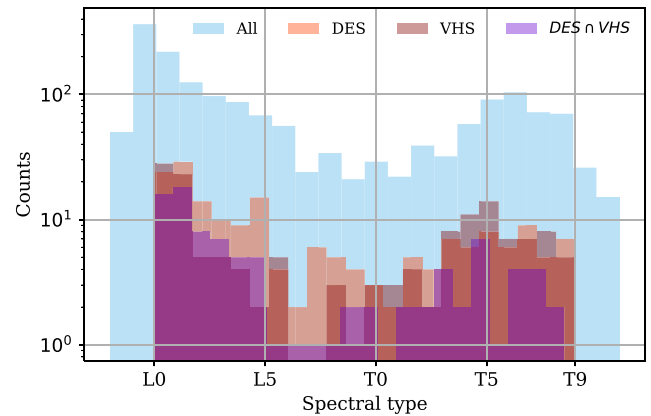


**Figure 2.** The distribution of known BDs in the Gagné sample for different overlaps. The original sample contains 1629 BDs, 208 of which are found in the DES Y3 data, 163 in the VHS DR3 data, and 104 in the  $\text{DES} \cap \text{VHS}$  data, after removal of M types and young L types.

of them ( $\approx 10$  per cent), there is a discrepancy of more than one spectral types, which can be considered as due to peculiarities. In these cases, we adopted the optical classification. We tested the effect of using one or another value in the creation of the templates and found discrepancies of  $\lesssim 3$  per cent.

From the initial list of 1772 BDs, we removed objects that are considered peculiar (in colour space) or that are part of a double system, categories given in the Gagné compilation and also sources with spectral type M, yielding a remaining list of 1629 BDs. From this list, 233 are present in the DES footprint, but when we match at 2 arcsec between the DES and Gagné sample, we only recover 150 of these. For the remaining 83 that are not matched within 2 arcsec, we visually inspected the DES images to find their counterparts beyond the 2 arcsec radius, recovering in this process 58 additional LT types to the DES sample. Therefore, our sample totals 208 known LT dwarfs, while 25 are not found due to partial coverage of the footprint or due to high proper motions.

Repeating the same procedure but for VHS: in the entire VHS footprint (not only in the  $\text{DES} \cap \text{VHS}$  region), but we find 163 LT dwarfs at 2 arcsec radius. Here we did not repeat the process of manually recovering missing objects. In the  $\text{DES} \cap \text{VHS}$  region, we end with 104 confirmed LT dwarfs, from 139 in the  $\text{DES} \cap \text{VHS}$  common footprint. The missing sources are due to the same effects of partial coverage or high proper motions.

During our analysis, we found that BDs tagged as ‘young’ in the Gagné sample were biasing the empirical colour templates used for classification (see details in Section 5.1). BDs are tagged as ‘young’ in the Gagné sample whenever they are found as members of a Young Moving Group or are otherwise suspected of having ages less than a few 100 Myr. Young BDs are typically found to exhibit redder photometric colours in the near-infrared due to the effects of low-gravity and/or different cloud properties (e.g. Faherty et al. 2016). We, therefore, removed those from the calibration sample.

As a result, our final LT calibration sample contains 208 sources in the Y3 DES sample, 104 in the  $\text{DES} \cap \text{VHS}$  region, 163 in VHS DR3 alone, and 128 with  $\text{VHS} \cap \text{AllWISE}$ . These are the final samples we use to calibrate the empirical colour templates for BDs, depending on the colour to parametrize. [For example, for  $(J - H)$  we use the VHS sample with 163 sources, whereas for  $(i - z)$  and  $(z - Y)$ , we use the DES sample with 208 sources.] These templates will also feed the *GalmodBD* simulation for the LT population (Section 8).

In Fig. 2 we show the number of BDs as a function of the spectral

<sup>8</sup><https://jgagneastro.wordpress.com/list-of-ultracool-dwarfs/>

type in the Gagné sample, matched to different photometric data. At this point, we assume that the colour templates we will obtain from these samples are representative of the whole BD population. Later, in Section 4, we will compare the target sample to the calibration sample and confirm that this approximation is valid.

### 3.2 M dwarfs

The sample of M dwarfs comes from a spectroscopic catalogue of 70 841 visually inspected M dwarfs from the seventh data release of the SDSS (West et al. 2011), confined to the Stripe82 region. After matching with the target sample at a 2 arcsec radius, we end up with 3849 spectroscopically confirmed M dwarfs with spectroscopic classification, from M0 to M9. We use this sample to create templates for our classification schema, with particular care for the transition from M9 to L0. These templates will also feed the *GalmodBD* simulation for the M population (Section 8).

### 3.3 Quasars

Quasars have been traditionally a source of contaminants in BD searches since they are point-like, and at high redshift, they can be very red, especially in infrared searches using WISE or 2MASS data, for instance. On the other hand, this degeneracy can be broken with the use of optical information, as shown in Reed et al. (2015, 2017). We use two samples of confirmed quasars in DES, one from Tie et al. (2017) up to  $z = 4$  and the one from Reed et al. (2017) with  $z > 6$ . In principle, quasars follow a different colour locus [as seen in Reed et al. (2017)] but some contamination might remain after the colour cuts, and we will treat them as a source of extragalactic contamination in Section 6.1.

### 3.4 Colour templates

To define our colour selection, to classify BDs, and to produce realistic colours in the simulation, we create colour templates as a function of the spectral type in  $(i - z)_{AB}$ ,  $(z - Y)_{AB}$ ,  $(Y_{AB} - J_{Vega})$ ,  $(J - H)_{Vega}$ ,  $(H - K_s)_{Vega}$ ,  $(K_s - W1)_{Vega}$ , and  $(W1 - W2)_{Vega}$ .

Since M dwarfs are much more abundant than BDs in our samples, we adopt different approaches to build the colour templates, depending on the available number of calibrating sources. For M and L0 dwarfs, where we have enough statistics, we take the mean value for each spectral type as the template value, selecting sources with  $SNR > 5\sigma$  only. Beyond L0, since we do not have enough statistics for all spectral types, we follow a different approach: we fit the colour versus spectral type distribution locally in each spectral type using both first-order and second-order polynomials. For instance, for L7 we fit the colour distribution between L3 and T3, and with the given first-order and second-order polynomials, we interpolate the result for L7. Finally, the colour value for the given spectral type is taken as the average of the two polynomial fits.

The empirical templates can be seen in Fig. 3. The template values are listed in Table 3. We found several degeneracies in colour space. For example, in  $(H - K_s)$ , one cannot distinguish spectral types between early L and late L/early T because their colours are the same, or in  $(W1 - W2)$ , where we cannot discriminate between mid-M stars and early-mid/L dwarfs for the same reason. Since several colours exhibit degeneracies in their colour-spectral type relationships, it is important to have multiple colours to establish a good spectral type calibration and therefore the need for a combination of optical and infrared data.

In terms of the dispersion about the templates, it increases with spectral type, with some exceptions. For example, in  $(W1 - W2)$  the dispersion for M types is larger than for some LT types. In the T regime, in general, the dispersion due to variations in metallicity, surface gravity or cloud cover, among other effects, can be of the same order or bigger than the dispersion introduced by differences in SNR. Possible peculiar objects will be identified with high  $\chi^2$  when compared to the empirical templates.

In the last panel of Fig. 3, we compare all the templates together. From here, we find that  $(i - z)$  colour has the largest variation through the ML range, demonstrating the importance of the optical filters to separate M dwarfs from LT dwarfs.  $(W1 - W2)$  is very sensitive to T types (as expected by design), and  $(Y - J)$  is also important for the ML transition. The other bands will add little to the M/L transition, but they will help on L/T transition. Similar findings were already presented in Skrzypek et al. (2015).

We have compared our template values to those in Skrzypek et al. (2015) and to those in Filippazzo et al. (2015). The agreement is, in general, very good, with some tensions in the L6–T3 regime and in T7–T9 regime that we account for the fact that calibration samples are sparse for these spectral types in all references, reflecting our ignorance about these spectral types. Also, the photometric systems of these two references are not exactly the same as ours, so part of the difference also comes from it. In any case, we do not find any striking differences, and the overall shape of our templates agrees with the aforementioned references. We have tested using different template distributions in the classification process and results are robust with respect to these changes.

## 4 MLT COLOUR SELECTION

In this section we explain the steps to select our initial list of LT candidates from the target sample. In Fig. 4, we show the colour–colour diagrams of known BDs, M dwarfs, and quasars. Clearly, some of these colour–colour diagrams are more efficient to disentangle LT dwarfs from other point sources than others. Furthermore, at  $z \sim 22$ , we are still mostly complete in the  $i$  band, although not necessarily for late T types. Therefore we do not demand detection in  $i$  band, but we still impose a minimum  $(i - z)$  colour as a selection criterion, very efficient to remove quasars from our sample, as attested by Fig. 4.

The nominal cut at  $z_{AB} = 22$  is set to ensure that the combination  $DES \cap VHS$  takes full advantage of both surveys, something that was not possible earlier due to the brighter magnitude limits imposed by SDSS. At  $z_{AB} = 22$ , we are limited at  $J_{Vega} \sim 19.7$ . This corresponds to  $z_{AB} - J_{Vega} \sim 2.30$ , which is the colour of an L0 according to the templates presented in Table 3. This is brighter by at least 0.7 magnitudes than the  $5\sigma$  limit on VHS. In other words, we will be able to reach  $z_{AB} = 22.7$  in upcoming DES updates and still remain complete in optical and VHS bands for the LT types. The magnitude limits on VHS bands are also deeper than its predecessors. For example, UKIDSS has a global depth limit of  $J_{Vega} \sim 19.6$  (Warren et al. 2007), while VHS has  $J_{Vega} \sim 20.3$ .

We define the colour space where BDs are found to reside. We initially aim at high completeness in colour space, at the expense of allowing for some contamination by M dwarfs and extragalactic sources. Purity is later improved at the classification stage (Section 5).

The entire selection process can be summarized in seven stages as detailed below and listed in Table 4:

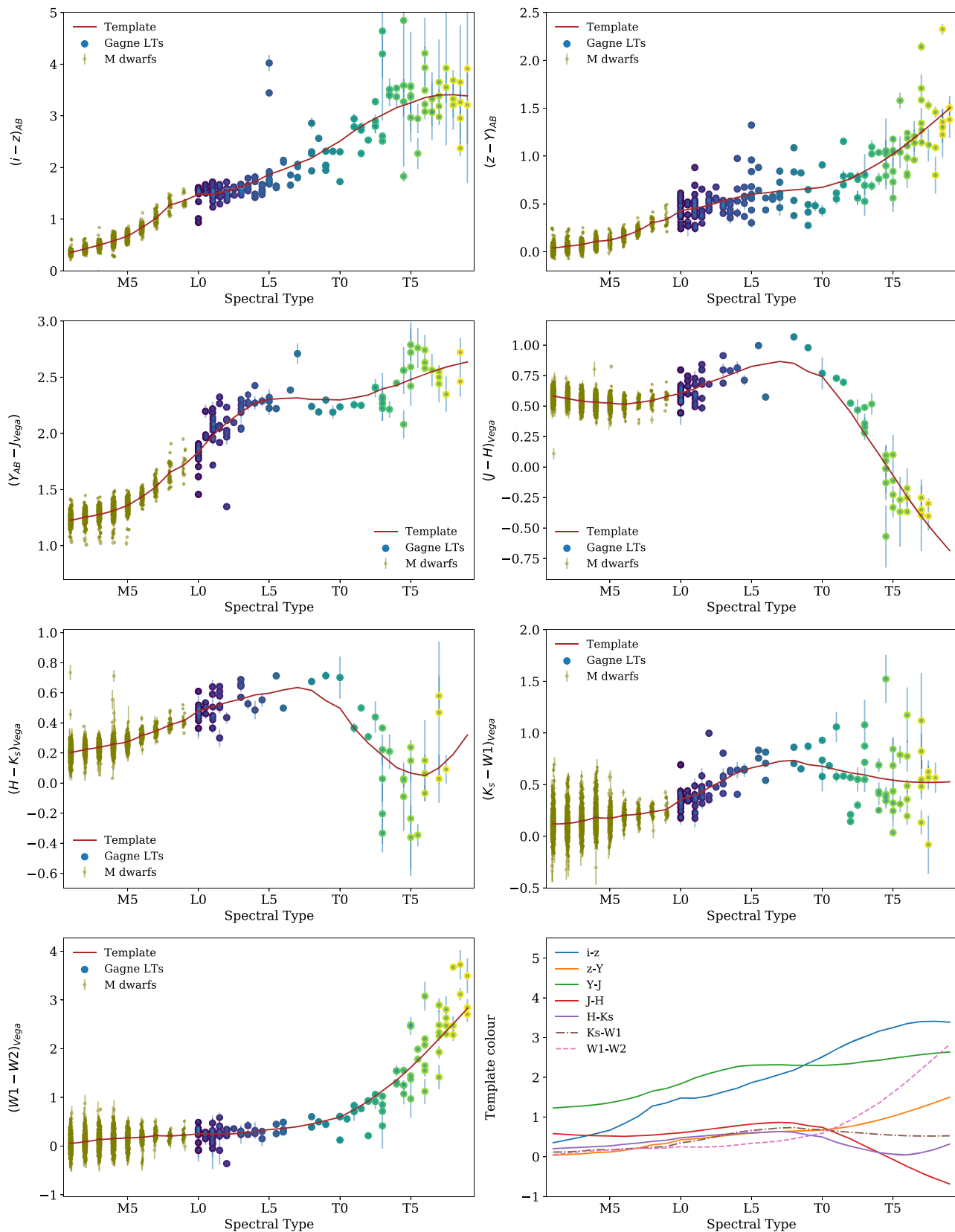


**Figure 3.** Colours as a function of the spectral type in the MLT spectral regime. M dwarfs are shown in olive, in blue, green, and yellow are BDs with their colour given by their spectral type, as seen in Fig 4. These templates are used during the classification and to feed the *GalmodBD* simulations. In the last panel, we compare all the templates together. Since several colours exhibit degeneracies in their colour-spectral type relationships, it is essential to have multiple colours to establish a good spectral type calibration.

**Table 3.** Template values as a function of the spectral type in the MLT regime. These are the best-fitting values shown in Fig. 3 and that are later used in the classification and to feed the *GalmodBD* simulation.

Spectral type	Colour						
	$(i - z)_{AB}$	$(z - Y)_{AB}$	$(Y_{AB} - J)_{Vega}$	$(J - H)_{Vega}$	$(H - K_s)_{Vega}$	$(K_s - W1)_{Vega}$	$(W1 - W2)_{Vega}$
M1	0.35	0.04	1.23	0.58	0.20	0.12	0.05
M2	0.43	0.06	1.25	0.56	0.22	0.12	0.09
M3	0.50	0.07	1.28	0.54	0.24	0.14	0.13
M4	0.58	0.11	1.31	0.53	0.26	0.18	0.15
M5	0.67	0.12	1.36	0.52	0.27	0.17	0.17
M6	0.83	0.16	1.43	0.51	0.31	0.20	0.18
M7	1.02	0.22	1.52	0.53	0.34	0.21	0.21
M8	1.27	0.30	1.65	0.54	0.39	0.24	0.21
M9	1.36	0.34	1.72	0.58	0.42	0.26	0.22
L0	1.48	0.43	1.83	0.60	0.48	0.35	0.25
L1	1.47	0.45	1.98	0.64	0.51	0.40	0.24
L2	1.53	0.49	2.09	0.69	0.54	0.47	0.25
L3	1.63	0.53	2.19	0.73	0.56	0.54	0.26
L4	1.73	0.57	2.27	0.78	0.59	0.62	0.30
L5	1.87	0.60	2.30	0.82	0.60	0.66	0.34
L6	1.96	0.62	2.31	0.84	0.62	0.69	0.36
L7	2.07	0.63	2.32	0.87	0.64	0.72	0.40
L8	2.18	0.65	2.30	0.85	0.62	0.73	0.46
L9	2.35	0.66	2.30	0.78	0.55	0.69	0.52
T0	2.51	0.67	2.30	0.74	0.50	0.68	0.59
T1	2.71	0.72	2.32	0.60	0.36	0.64	0.75
T2	2.88	0.76	2.34	0.45	0.26	0.61	0.92
T3	3.02	0.84	2.40	0.27	0.18	0.59	1.13
T4	3.16	0.92	2.43	0.11	0.10	0.56	1.35
T5	3.25	1.02	2.48	-0.07	0.07	0.54	1.62
T6	3.35	1.13	2.53	-0.24	0.05	0.53	1.90
T7	3.40	1.25	2.57	-0.40	0.10	0.52	2.21
T8	3.41	1.37	2.61	-0.55	0.20	0.52	2.51
T9	3.39	1.50	2.64	-0.68	0.32	0.53	2.83

(i) Quality cuts on DES and matching to VHS (explained in Section 2). We end up with 42 046 583 sources after applying a matching within 2 arcsec between the DES and the VHS, and selecting sources with `SEXTRACTOR_FLAGS.z, Y = 0` and `IMAFLAGS_ISO.i, z, Y = 0`.

(ii) Magnitude limit cut in  $z < 22$  and SNR greater than  $5\sigma$  in  $z, Y, J$ . We end up with 28 259 901 sources.

(iii) We first apply a cut in the optical bands ( $i - z$ ), removing most quasar contamination while maintaining those sources for which  $i$  band has no detection. We decided to apply a cut of  $(i - z) > 1.2$ . In comparison with previous surveys, as seen in Table 1, this is a more relaxed cut, initially focusing on high completeness in our sample at the expense of purity. This cut eliminates more than 99.8 per cent of the catalogue, leaving us with a sample of 65 041 candidates.

(iv) We apply a second selection to the target sample in the space  $(z - Y)$  versus  $(Y - J)$ . From Fig. 4, we decided the cut to be:  $(z - Y) > 0.15$ ,  $(Y - J) > 1.6$  avoiding the  $z > 6$  QSO colour locus. The surviving number of sources is 35 548. This cut is actually very similar to the cut proposed in Skrzypek et al. (2016). They imposed  $Y - J > 0.8$  (Vega). Transforming our  $Y$  band to Vega, our equivalent cut would be  $Y - J > 0.7$ .

(v) Finally, we apply the footprint mask. In this process, we end up with 35 426 candidates. This is the sample that goes into classification. Extragalactic contamination is treated after running the classification.

(vi) Apply the *phototype* method (Skrzypek et al. 2015) to estimate the spectral type in the MLT range for all the targets.

We call this method *classif* (see Section 5). After removal of the M types, we ended with 12 797 LT types.

(vii) Removal of extragalactic contamination (see Section 6.1). We end up with the final sample of 11 745 LT types from which 11 545 are L types, and 200 are T types. There is also extragalactic contamination in the M regime, as explained in the next section.

## 5 SPECTRAL CLASSIFICATION

In this section we explain the method to assign spectral types to our candidate list and evaluate its uncertainties based on the calibration samples. We implement the same classification method presented in Skrzypek et al. (2015, 2016), based on a minimization of the  $\chi^2$  relative to the MLT empirical templates. Our method uses the templates created in Section 3.4. We refer to our classification code as *classif*.

As mentioned earlier, we impose a  $5\sigma$  detection in  $z, Y, J$ . For the rest of the bands, we require a  $3\sigma$  detection. If the magnitude error exceeds this limit, we consider the source as not observed in the given band. However, there is one exception, the  $W1$  magnitude, which is cut at  $5\sigma$  in the AllWISE catalogue.

Let a set of  $N_{\text{bands}}$  observed for the  $j$ -th target to be  $\{m_{ji}, i = 1, N_{\text{bands}}\}$  and their photometric uncertainties be  $\{\sigma_{m_{ji}}, i = 1, N_{\text{bands}}\}$ . Let also a set of colour templates be  $\{c_{i,k}, i = 1, N_{\text{bands}}, k = 1, N_{\text{spectype}}\}$ , which give the magnitude difference between band  $b$  and the reference band  $z$  for each spectral type. Hence  $c_{z,k} = 0$  by construction. Let us consider the template intrinsic dispersion to be  $\{\sigma_{c_{i,k}}, i = 1, N_{\text{bands}}, k = 1, N_{\text{spectype}}\}$ , which we fix for all bands and



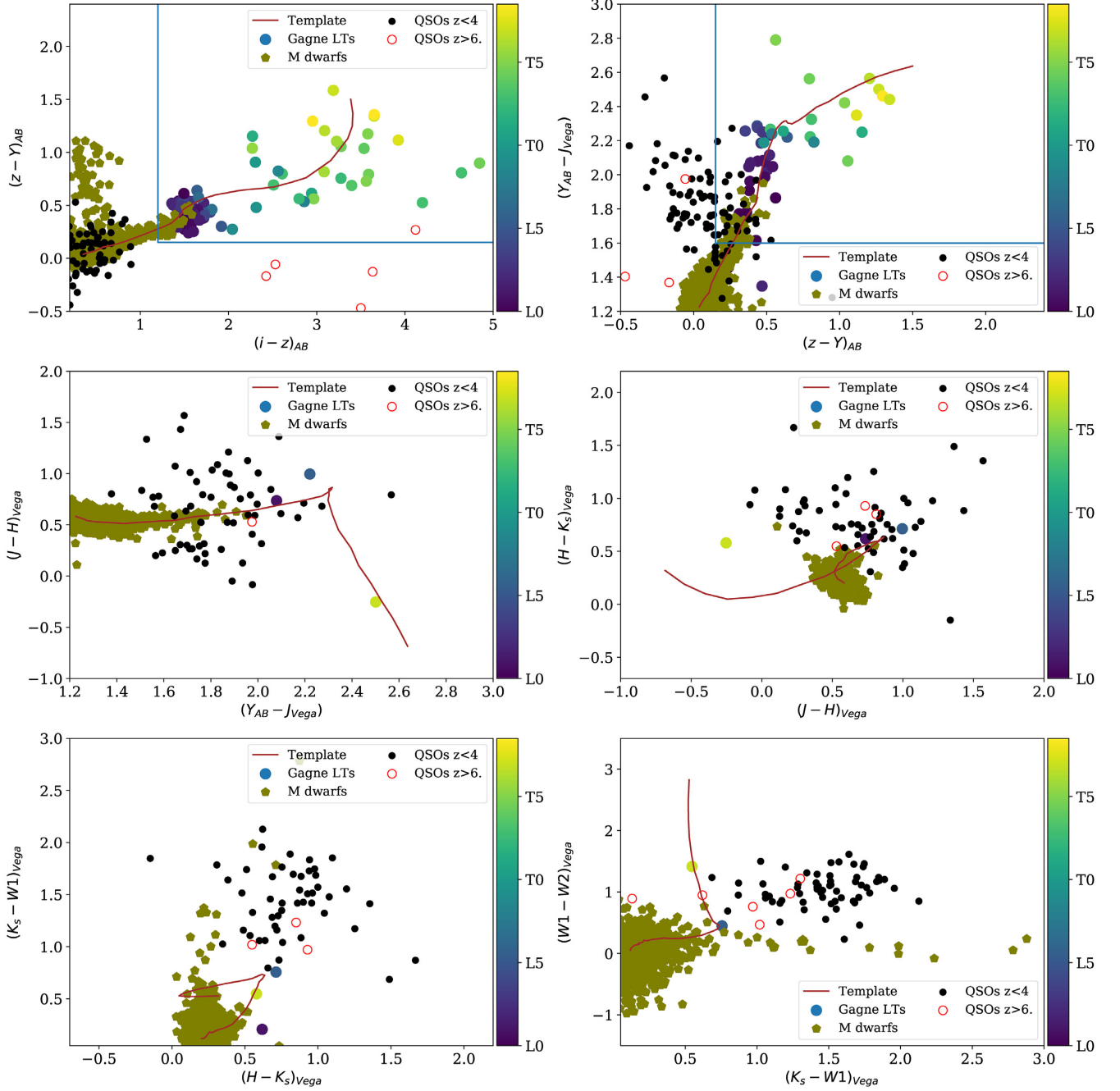


**Figure 4.** Colour–colour diagrams for spectroscopically confirmed BDs, M dwarfs, and quasars that are found in the target sample. Each panel corresponds to a specific colour–colour space. In all panels, M dwarfs are shown as olive circles. Quasars as black circles for  $z < 4$  and as empty red circles for  $z > 6$ , whereas LT dwarfs are shown as filled circles with their colour a function of the spectral type, as depicted in the colour bar on the right. The colour templates that were empirically derived (see Section 3.4) are shown by the brown line. The colour cuts applied to the sample before classification are depicted by the blue lines in the first two panels.

templates to  $\sigma_c = 0.07$ , as also done by Skrzypek et al. (2016). The total error for band  $b$ , for the  $j$ -th target will be  $\sigma_{bj} = \sqrt{\sigma_{m_{jb}}^2 + \sigma_c^2}$ .

The first step in the classification process for the  $j$ -th target is, for each of the  $k$ -th spectral type ( $N_{\text{spectype}}$ ), to calculate the inverse variance weighted estimate of the reference magnitude (in our case  $z$ ) as

$$\hat{m}_{j,z,k} = \frac{\sum_{b=1}^{N_{\text{bands}}} \frac{m_{jb} - c_{bk}}{\sigma_{bj}^2}}{\sum_{b=1}^{N_{\text{bands}}} \frac{1}{\sigma_{bj}^2}}. \quad (1)$$

Next, the above value is used to calculate the  $\chi^2$  value for the  $k$ -th spectral type, for each  $j$ -th target:

$$\chi^2(\{m_j\}, \{\sigma_{bj}\}, \hat{m}_{z,k}, k) = \sum_{b=1}^{N_{\text{bands}}} \left( \frac{m_{jb} - \hat{m}_{z,k} - c_{b,k}}{\sigma_{bj}} \right)^2. \quad (2)$$

Finally, we assign the spectral type that gives the minimum  $\chi^2$  value.

**Table 4.** Steps used in this paper to classify LT sources in  $\text{DES} \cap \text{VHS} \cap \text{WISE}$ . First, quality cuts are applied to the data to remove spurious targets. Next, a magnitude limit is imposed in the  $z$  band and finally, colour cuts are applied to select only the reddest objects. These are the sources that enter the classification. Finally, extragalactic contamination is removed.

Step	Description	Percentage removed	Number remaining
0	DES Y3 sample (DR1)		399 263 026
1	Matching 2 arcsec to VHS FLAGS <sub>z, Y</sub> = 0 IMAFLAGS_ISO.i, z, Y = 0	89.5	42 046 583
2	$z < 22$ $\text{SNR}_{-z, Y, J} > 5\sigma$	33	28 259 901
3	$(i - z)_{\text{AB}} > 1.2$	99.8	65 041
4	$(z - Y)_{\text{AB}} > 0.15$ $Y_{\text{AB}} - J_{\text{Vega}} > 1.6$	45	35 548
5	Footprint masking	0.3	35 426
6	LT classification	64	12 797
7	Remove extragalactic contamination	8	11 745

### 5.1 Classification performance on known samples

In this section we apply *classif* to our list of known BDs and M dwarfs to assess how well the method works. We run the code on the Gagné list of 104 known BDs (including young BDs) and in the West list of known M dwarfs. Results are summarized in Fig. 5, where we show the photometric spectral type versus the spectroscopic classification, separately for M (left) and LT types (right). In these figures, the diamond points are those where the difference between the true spectral type and the photometric estimation is greater or equal to 4 ( $\Delta_t \geq 4$ ). There are eight sources with  $\Delta_t \geq 4$ , from which six of them are young L types.

We estimate the accuracy of the method using

$$\sigma_{\text{classif}} = \frac{\sum_{j=1}^{N_{\text{candidates}}} |\Delta_t|}{N_{\text{candidates}}} \frac{\sqrt{2N_{\text{candidates}}}}{2}. \quad (3)$$

Dividing in M types (from West sample), L and T types (Gagné sample), we get  $\sigma_M = 0.69$  (for M with spectral type M7 or higher),  $\sigma_L = 1.47$  and  $\sigma_T = 1.12$  and a global  $\sigma_{\text{LT}} = 1.37$ . If we now estimate the errors but without the young L types, the metrics improve to  $\sigma_L = 1.03$  and  $\sigma_T = 1.12$  and a global  $\sigma_{\text{LT}} = 1.06$ , a precision compatible to what was found in Skrzypek et al. (2016). None the less, it is obvious from Fig. 5 that it is much more appropriate to use a  $3\sigma$  value for how well one establish a photometric spectral type for these low-mass objects, thereby implying that the best one can do in estimating photometric spectral types is  $\pm 2$  for M types and  $\pm 3$  for LT-dwarfs. Likewise, we have not found any dependence on SNR or brightness of the calibration source.

Another test we perform is to estimate the spectral types for those LT candidates in the overlapping sample with Skrzypek et al. (2016), consisting of 74 sources. We run *classif* on these 74 sources and compare both photometric estimators. In general, we find an excellent agreement with  $\sigma_{\text{classif, skrzypek}} = 0.38$ . In Fig. 6 we show the comparison between the two methods.

## 6 CLASSIFICATION OF THE TARGET SAMPLE

After confirming that our method reliably classifies MLT spectral types, we run *classif* on the target sample presented in Section 4, a sample of 35 426 candidates. A visual inspection of the candidates demonstrates that all are real sources. The main caveat in our methodology might be residual contamination by extragalactic sources. We next explain our star–galaxy separation method.

### 6.1 Extragalactic contamination

To remove possible extragalactic contamination, we run LEPHARE photo- $z$  code on the whole candidate list using galaxy and quasar templates spanning various redshifts, spectral types, and internal extinction coefficients (the LEPHARE configuration used is presented in Appendix A). For those candidates where the best fit is  $\chi_{\text{lephare}}^2 < \chi_{\text{classif}}^2$ , we assign them a galaxy or quasar class and are no longer considered MLT types. This method also has the potential to identify interesting extragalactic targets.

It is worth noting that running LEPHARE on the Gagné sample, we can recover most known LT types. Only one BD in the Gagné sample is assigned a galaxy class, which is already known to be a very peculiar L7 type called *ULAS J222711–004547* (Marocco et al. 2014). It has a  $\chi_{\text{classif}}^2 > 630$ , while the rest of the 103 BDs have a  $\chi_{\text{classif}}^2 < 130$ . Also, the classification is robust concerning changes in the galaxy libraries used in the LEPHARE configuration: we tested various choices of galaxy templates, and the number of extragalactic contaminants remained constant within errors.

### 6.2 Results

After running *classif* and LEPHARE on the target sample, we obtain 32 608 sources classified as MLT types. From these, 20 863 are M types, 11 545 are L types, and 200 are T types. Our catalogue also includes 2818 candidates classified as galaxies or quasars. A preliminary discussion about the properties of the extragalactic sources is given in Appendix B. In Section 7 we show an example of the data published in electronic format and its explanation. It consists of a table with all the 11 745 candidates in the target sample with LT spectral type including the photometry used and the *classif* results.

Sources with a number of bands available for classification (NBANDS) less than 5 (3 or 4) are generally assigned to extragalactic spectral types; likewise those have the best-fitting MLT template as M types. By visually inspecting the spectral energy distribution of sources with NBANDS < 5, compared to the best-fitting templates of MLT types, galaxies, and quasars, we conclude that the classification is ambiguous and should be taken with caution when NBANDS < 5. From the catalogue of 35 426 targets, 6 per cent have NBANDS < 5. If we consider only those with spectral type L, the percentage goes down to 3.7 per cent (469 targets), i.e. 3.7 per cent of the L types have NBANDS < 5, from which 96 per cent (449 targets) are assigned to a galaxy template instead of to an L type. This effect contributes to the uncertainty associated with the removal of extragalactic contamination.

At this point, we compare the colour distribution as a function of the spectral type for the target sample with respect to the empirical templates of Section 3.4. We assumed that the templates were representative of the LT population. In Fig. 7 we can see the comparison. Our modelling reproduces the target sample colour distribution. Only in the late L and late T regime, we find some

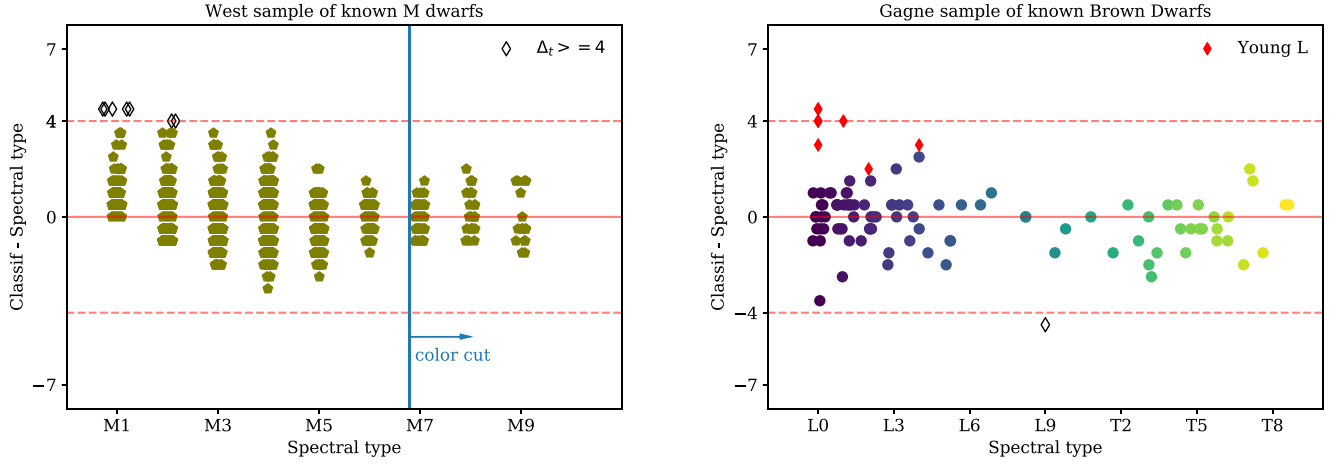


**Figure 5.** Classification performance for M dwarfs (left) and LT types (right). In both panels, sources with a misclassification higher or equal 4 are shown as diamond symbols. Red dashed lines indicate the limits where the difference between the spectroscopic and photometric classification is equal to 4. On the right-hand panel, we also tag young L types, which were not used to build the templates but are shown here to illustrate their peculiar nature, with a classification that is always higher than 2. The classification have a mean uncertainty of  $\sigma_M = 0.69$  (for M dwarfs passing the colour cuts) and  $\sigma_L = 1.03$  and  $\sigma_T = 1.12$  for the LT sample without the young L types. For visualization purposes we have applied small random shifts smaller than  $\Delta_{\text{template}} \pm 0.3$  to the true spectral types (only in the x-axis).

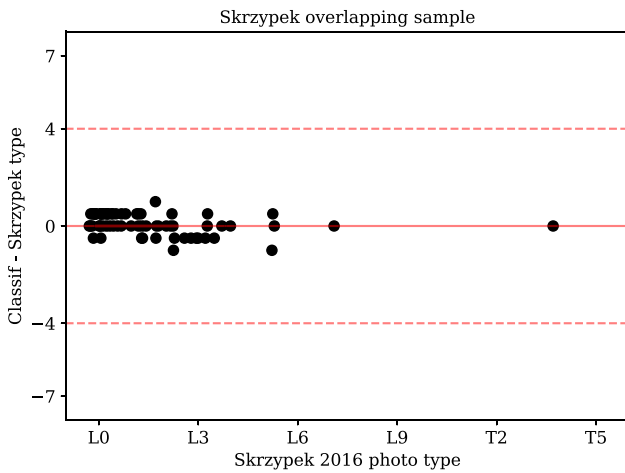


**Figure 6.** Comparison between the photometric classification of Skrzypek et al. (2016) and *classif* for 74 common LT candidates found in the footprint. We find an excellent agreement between both estimates with a mean dispersion of  $\sigma_{\text{classif}} = 0.38$ . For visualization purposes we have applied small random shifts smaller than  $\Delta_{\text{template}} \pm 0.3$  to the x-axis.

discrepancies. This effect is due to both the lack of statistics when we calculated the empirical templates in these regimes, and to the intrinsic dispersion in colours, as attested by our comparison to Filippazzo et al. (2015) and Skrzypek et al. (2015) described in Section 3.4.

### 6.3 Photometric properties of the LT population

We analyse the properties of the 11 745 LT types found in the target sample. The distribution of spectral types can be found in Fig. 8 in logarithmic scale. In Fig. 9 we show the distribution of bands available for classification.

The  $\chi^2_{\text{classif}}$  of the fits are generally very good, in agreement with the theoretical curve for the same degrees of freedom. In our model we have two free parameters, the brightness of the source

and the spectral type, therefore the degrees of freedom are  $N_{\text{bands}} - 2$ . The  $\chi^2_{\text{classif}}$  distribution can be found in Fig. 10. The theoretical curve is a summation over the  $\chi^2$  curves for degrees of freedom 1,2,3,4,5 (corresponding to  $N_{\text{bands}} = 3, 4, 5, 6, 7, 8$ , respectively, where each curve was multiplied by the percentage of total sources with each number of bands). The reduced  $\chi^2$  defined as  $\frac{\chi^2}{(d.o.f.)}$  is close to one, with a mean value of  $\frac{\chi^2}{(d.o.f.)} = 1.3$  and a median value  $\text{med}(\frac{\chi^2}{(d.o.f.)}) = 0.95$ .

In our analysis, we tag BDs as peculiar (in terms of colours) if their  $\chi^2_{\text{classif}}$  is beyond 99.7 per cent of the probability, which in a  $z$ -score analysis means having a  $\chi^2_{\text{classif}} > 3\sigma$  off the median. In our case, we set the cut-off at  $3.5\sigma$  instead to accommodate the natural dispersion of LT types. Since the  $\chi^2_{\text{classif}}$  distribution is not normal we define  $\sigma$  based on the median absolute deviation (MAD) instead of the standard deviation, and since the distribution is non-symmetrical, we apply a double MAD strategy. Since T types have intrinsically more colour dispersion than L types, we treat them separately. Applying the double MAD algorithm to the  $\chi^2_{\text{classif}}$  distribution of L and T types, for a cut-off =  $3.5\sigma$ , we end up with 461 L types labelled as peculiar ( $\approx 4$  per cent) and 6 T types tagged as peculiar ( $\approx 3.5$  per cent). These limits are equivalent to say that L types are peculiar whenever their  $\chi^2_{\text{classif}} > 20$ , and that T types are peculiar whenever their  $\chi^2_{\text{classif}} > 46.5$ . Peculiar sources can be identified in the catalogue reading the PECULIAR column as explained in Section 7.

#### 6.3.1 Photometric distances

We estimate photometric distances using the distance modulus:

$$d(\text{Type})[i] = 10 \times 10^{(m_z[i] - M_z(\text{Type}))/5}. \quad (4)$$

Absolute magnitudes have been anchored to  $M_{W1}$  and  $M_{W2}$  from Dupuy & Liu (2012) as explained in Section 8.1. We compare two estimates for the distance: one where we use all available bands from the  $i, z, Y, J, H, K_s, W1, W2$  set, and then we average over the bands to give a mean value, and the other where we use band  $z$  only.

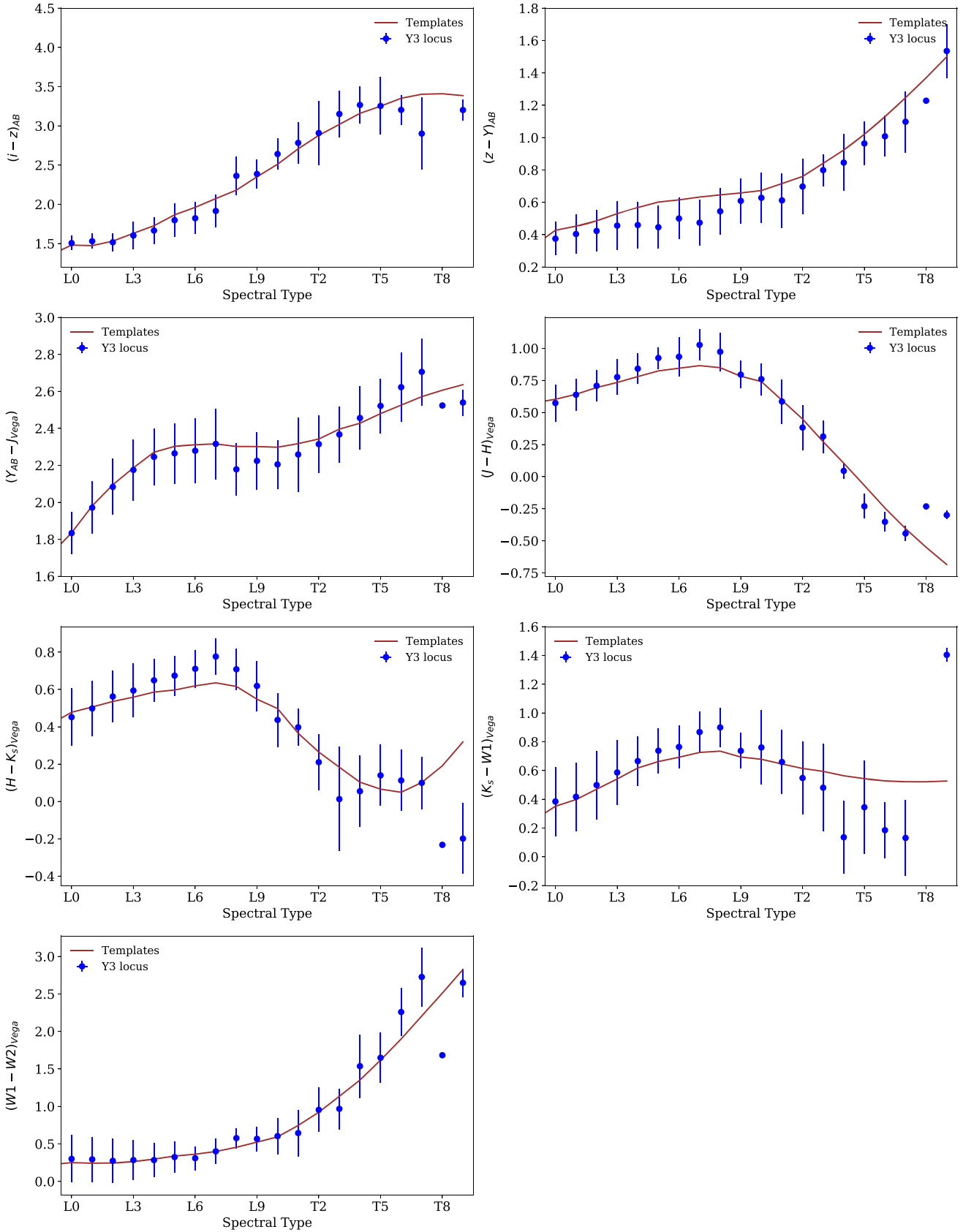


**Figure 7.** Comparison between the colour templates and the locus of the LT candidates. Blue points show the mean and standard deviation colour for candidates with the given spectral type. In brown, the empirical templates used. The agreement is good through all the spectral space, with deviations appearing in the late L and late T type regime, where the calibration sample is sparse. In any case, these discrepancies are within errors and therefore, we confirm the initial assumption that the calibration sample is representative of the whole LT population.



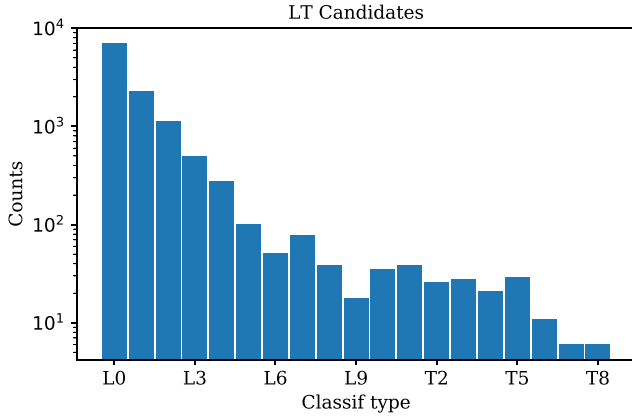


**Figure 8.** The distribution of spectral types for the LT candidates. We classify 20863 sources as M dwarfs (from M7 to M9, not shown here), 11545 as L types (from L0 to L9), and 200 as T types (from T0 to T9).

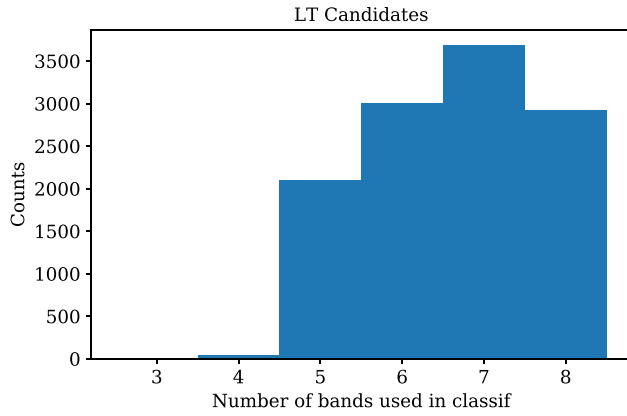


**Figure 9.** The number of bands ( $N_{\text{bands}}$ ) used during the classification. This information is used to assign weights when we calculate the theoretical  $\chi^2$  distribution in Fig. 10.

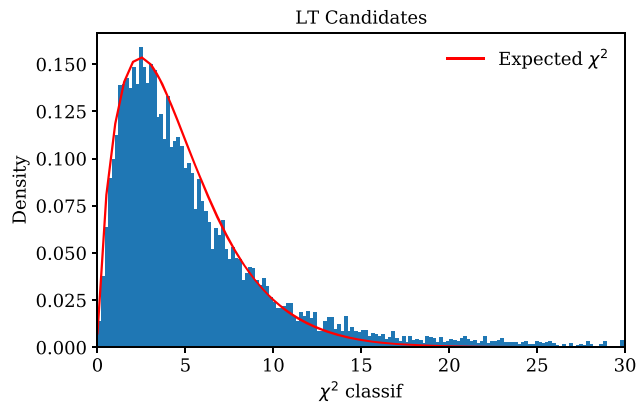


**Figure 10.**  $\chi^2$  distribution for the LT candidates, together with the theoretical expectation. In order to calculate this curve, we add, proportional to the numbers in Fig. 9, the degrees of freedom. Our distribution follows the expected curve, therefore our errors reflect the dispersion of the model. The reduced  $\chi^2$  defined as  $\frac{\chi^2}{(d.o.f)}$  is close to one, with a mean value of  $\frac{\chi^2}{(d.o.f)} = 1.3$  and a median value  $\text{med}(\frac{\chi^2}{(d.o.f)}) = 0.95$ .

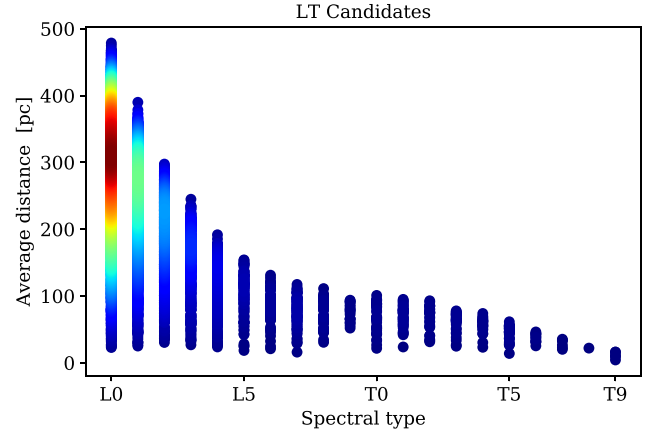


**Figure 11.** Distances as a function of spectral type. Distances have been calculated using the average value from the distance modulus obtained using all available bands. The colour scale represents the density. Most LT candidates are early L types (L0–L3) at distances smaller than 500 pc.

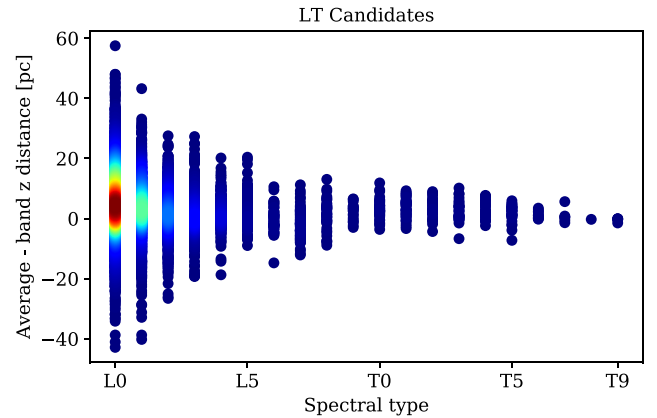


**Figure 12.** Difference between the two distance estimators. In one where we only use  $z$  band and another where the average value over all available bands is used. The colour scale represents the density.

The distance distribution can be found in Fig. 11 for the averaged value. In Fig. 12 we show the difference between the averaged value and the  $z$ -band estimate. In general, both definitions agree. In the published catalogue both estimates are given with names `DISTANCE_AVG` and `DISTANCE_Z`.

## 7 ELECTRONIC CATALOGUE

This is the largest photometric LT catalogue published to date, containing 11745 sources. We also publish the M dwarf catalogue in a separate table containing 20863 sources. Table 5, 6, and 7 shows a sample of the LT catalogue, which can be accessed at <https://des.nsa.illinois.edu/releases/other/y3-mlt>. The number of LT types found in the target sample is subject to completeness and purity effects (see Section 12).

Spectral type is given by `SPT_PHOT` with the following convention: L types are assigned `SPT_PHOT` from 10 to 19, corresponding to L0 to L9, and from 20 to 29 for the T types, corresponding with T0 to T9. In the M dwarf catalogue, M types are assigned `SPT_PHOT` from 6 to 9. We also give the  $\chi^2$  of the classification and the number of bands used with columns `XI2_CLASSIF` and `NBANDS`. Distances are provided with two estimates, one based on band  $z$  only

**Table 5.** Example of the LT catalogue published, distances, and peculiar flag are only present in the LT catalogue. SPT\_PHOT is the spectral type, NBANDS the number of bands used in classification, and XI2\_CLASSIF the  $\chi^2$  for the best fit in *classif*. DISTANCE\_AVG is the average distance calculated from apparent magnitudes in all the available bands (in parsecs) and DISTANCE\_Z the distance calculated from the apparent magnitude in DES z band (in parsecs). HPIX\_512 is the *Healpix* pixel ID for *order = Nest* and *nside = 512* and PECULIAR is a category given if it has a  $\chi^2 > 3.5\sigma$  MADs (1 = peculiar, 0 = no peculiar).

COADD_OBJECT_ID	RA	DEC	SPT_PHOT	NBANDS	XI2_CLASSIF	DISTANCE_AVG	DISTANCE_Z	HPIX_512	PECULIAR
293254901	16.568	-52.537	8	5	4.326	419.848	406.993	2240708	0
302513036	18.383	-51.732	10	5	5.944	277.501	270.822	2240815	0
232352550	23.216	-63.690	8	5	3.974	380.790	370.102	2142795	0
237139089	313.501	-60.505	8	5	1.837	582.501	555.256	2935140	0
204133552	322.767	-53.430	9	5	4.503	491.583	495.687	2939932	0
71547410	330.937	-57.231	10	7	3.993	308.368	306.911	2915933	0
185491825	315.506	-53.252	9	5	1.530	393.643	398.255	2945055	0
93231446	33.147	-51.827	8	7	0.971	262.541	259.220	2244895	0

**Table 6.** DES magnitudes are in AB. *i*, *z* are PSF magnitudes from 'SOF' while *Y* band is from 'SEXTRACTOR'. VHS magnitudes are in Vega and are aperture magnitudes at 2 arcsec.

PSF_MAG_I	PSF_MAG_J	PSF_MAG_Z	PSF_MAG_Y	AUTO_MAG_Y	AUTO_MAG_Z	AUTO_MAGERR_Y	AUTOMAG3	JAPER3ERR
21.971	0.029	20.735	0.016	20.580	0.088	0.088	18.937	0.039
22.571	0.041	20.937	0.022	20.394	0.068	0.068	18.722	0.037
21.738	0.028	20.529	0.014	20.292	0.088	0.088	18.588	0.050
22.800	0.055	21.410	0.040	21.156	0.159	0.159	19.466	0.086
22.893	0.051	21.603	0.031	21.389	0.172	0.172	19.693	0.108
22.736	0.043	21.209	0.027	20.882	0.088	0.088	18.803	0.055
22.488	0.033	21.128	0.018	20.768	0.089	0.089	18.949	0.055
21.069	0.013	19.756	0.007	19.467	0.029	0.029	17.857	0.031

**Table 7.** VHS magnitudes are in Vega and are aperture magnitudes at 2 arcsec. WISE magnitudes are in Vega and are magnitudes measured with profile-fitting photometry. For more details visit <https://des.ncsa.illinois.edu/releases/other/y3-mlt>.

HAPERMAG3	HAPERMAG3ERR	KSAPERMAG3	KSAPERMAG3ERR	WIMPRO	W1SIGMPRO	W2MPRO	W2SIGMPRO
-9999	-9999	17.921	0.105	-9999	-9999	-9999	-9999
-9999	-9999	17.773	0.108	-9999	-9999	-9999	-9999
-9999	-9999	17.937	0.156	-9999	-9999	-9999	-9999
-9999	-9999	18.868	0.329	-9999	-9999	-9999	-9999
-9999	-9999	18.266	0.178	-9999	-9999	-9999	-9999
18.309	0.078	17.860	0.106	17.604	0.175	17.292	-9999
-9999	-9999	18.098	0.157	-9999	-9999	-9999	-9999
-9999	-9999	16.835	0.060	16.702	0.071	16.476	0.189

(DISTANCE\_Z) and another based on the average of the distances calculated in all the available bands (DISTANCE\_AVG). We also tag if the source is peculiar based on a  $z$ -score analysis of its  $\chi^2$ , where PECULIAR = 1 is peculiar and PECULIAR = 0 is not. Distances and the peculiar tag are only present in the LT catalogue. The LT and the M catalogues also include  $i$ ,  $z$ ,  $Y$  magnitudes from DES,  $J$ ,  $H$ ,  $K_s$  from VHS and  $W1$ ,  $W2$  from AllWISE as used in the classification. DES magnitudes are corrected with updated zeropoints different from those present in the public DR1 release (Dark Energy Survey Collaboration 2018) and they will be published in the future.

We matched the M and LT catalogues with *Gaia* DR2 release (Gaia Collaboration 2018), but the amount of matches was very low in the LT catalogue. Only 282 matches were found (2.4 per cent). In the M catalogue, we found 1141 matches (5.4 per cent), but these spectral types are not the scope of this paper.

## 8 MODELLING THE NUMBER COUNTS OF LT DWARFS

This section describes the effort to create robust expected number counts of LT dwarfs. The algorithm is called *GalmodBD*. It is a PYTHON code that computes expected galactic counts of LT dwarfs, both as a function of magnitude, colour, and direction on the sky, using the fundamental equation of stellar statistics. It was adapted from the code used by Santiago, Gilmore & Elson (1996) and Kerber, Javiel & Santiago (2001) to model *HST* star number counts, and by Santiago, Yanny & Yanny (2010) for a preliminary forecast of DES star counts. In the current analysis, we kept the density laws for the different Galactic components, and simply replaced the specific luminosity functions (LFs) of normal stars by the BD number densities as a function of the spectral type presented in Subsection 8.1.

*GalmodBD* also creates synthetic samples of LT dwarfs based on the expected number counts for a given footprint. Besides a model for the spatial distribution of BDs, *GalmodBD* uses empirically determined space densities of objects, plus absolute magnitudes and colours as a function of spectral type. The model is described in Section 8.1. The point generating process is described in Section 9. The validation tests are provided in Appendix D.

### 8.1 GalmodBD

For convenience, we will refer to the space density versus spectral type relation as the LF, which is somewhat of a misnomer, since luminosity does not scale uniquely with spectral type in the LT regime. We refer to the colours versus spectral type relations as C–T relation. The code requires several choices of structural parameters for the Galaxy, such as the density law and local normalization of each Galactic component. The density equations used to model the Milky Way are given in Appendix C, where we also show which parameters are held fixed, and which ones we allow to vary. For example, for the vertical density scale, we use an exponential law and we allow to vary the thin disc scale height. We use a de-projected de Vaucouleurs profile to describe the halo, that we keep fixed, since our sample is not sensitive enough to measure this component.

Equally crucial are parameters that govern the region of the sky and magnitude and colour ranges where the expected counts will be computed. These parameters are listed in different configuration files. Currently, only one choice of LF is available, taken from table 8 of Marocco et al. (2015). More specifically, for types earlier than L4, we use Cruz et al. (2007) space density values; from L4 to T5

**Table 8.** Number of BDs as a function of MW structural parameters in *GalmodBD*.  $h_{z,\text{thin}}$  is the thin disc scale height in parsecs,  $n_{\odot,\text{thick}}$  is the local thick-to-thin disc density normalization in percentage. The third column is the number of M types after the magnitude limit cut, the SNR cut and the colour cut. The fourth column is the number of LT types applying only the magnitude limit cut and the SNR cut and the fifth column is the number of early L types defined as those with spectral types less than L4. This last column will be compared with the number of BDs detected in our sample to give a first estimate of the thin disc scale height for early L types (L0–L3).

$h_{z,\text{thin}}$ (pc)	$n_{\odot,\text{thick}}$ (per cent)	M types [ $\text{snr} > 5\sigma$ + $z < 22$ + colour cut]	LT types [ $\text{snr} > 5\sigma$ + $z < 22$ ]	Early L types (L0–L3) (L0, L1, L2, L3)
250	5	11 609	8403	7427
250	10	12 869	9094	8055
250	15	14 121	9742	8663
250	20	15 428	10 475	9333
300	5	13 782	9426	8381
300	10	15 113	10 086	8992
300	15	16 366	10 821	9663
300	20	17 652	11 427	10 211
350	5	15 768	10 197	9118
350	10	17 018	10 887	9758
350	15	18 173	11 507	10 336
350	20	19 599	12 151	10 929
400	5	17 329	10 891	9798
400	10	18 611	11 590	10 454
400	15	19 968	12 313	11 079
400	20	21 345	12 958	11 684
450	5	18 831	11 463	10 343
450	10	20 015	12 022	10 873
450	15	21 486	12 774	11 575
450	20	22 653	13 384	12 115
500	5	20 231	11 891	10 764
500	10	21 425	12 589	11 409
500	15	22 732	13 255	12 028
500	20	24 086	14 100	12 785
550	5	21 217	12 297	11 152
550	10	22 551	13 038	11 811
550	15	23 859	13 763	12 501
550	20	25 121	14 359	13 033

we use those of Marocco et al. (2015) themselves, and for later types than T5 we use Burningham et al. (2013).

For the C–T relations, we first build absolute magnitude versus spectral type relations for AllWISE data.  $M_{W1}$ , and  $M_{W2}$  versus type relations are taken from figs 25, 26 and table 14 of Dupuy & Liu (2012). Once we anchor absolute magnitudes in these bands, we use the C–T relations found in Section 3 in Table 3, Fig. 3 to populate  $M_i$ ,  $M_z$ ,  $M_Y$ ,  $M_J$ ,  $M_H$ ,  $M_K$ .

The expected number counts are computed by direct application of the fundamental equation of stellar statistics. In summary, given a choice of apparent magnitude range in some filter, and some direction in the sky (pointer), we go through distance steps and for each of them, find the range of LT spectral types whose absolute magnitudes fit into the chosen apparent magnitude range. We then compute the volume element in the selected direction and distance and multiply it by the appropriate LF value.

The final number count as a function of apparent magnitude is the sum of these contributions for all appropriate combinations of spectral types (through their associated absolute magnitudes) and distances. Because we also have colour versus type relations, we can also perform the same integral over distance and type range to compute number counts as a function of colour.

*GalmodBD* incorporates extinction and dereddened using the Schlegel et al. (1998, SFD98) dust maps, although it can also

use (Burstein & Heiles 1982) maps. Conversion from  $A_V$  and  $E(B - V)$  to SDSS  $A_i$ ,  $A_z$ , and  $E(i - z)$  are based on An et al. (2008). None the less, in this first application of the code, we have not included any reddening effect since our sample is concentrated in the solar neighbourhood.

The code currently permits many choices of magnitudes and colours for number counts modelling, including colours in SDSS and DES in the optical, VHS and 2MASS in the near-infrared and AllWISE in the infrared.

In Appendix D we validate the *GalmodBD* simulation comparing its predictions with a prediction based on a single disc component analytical count.

## 9 SYNTHETIC CATALOGUES

Besides determining expected  $N(m)$  and  $N(\text{col})$  for BDs within some magnitude range and over some chosen area on the sky, the code also generates synthetic samples based on these number counts. This is done for every chosen direction, distance, and type (absolute magnitude) by randomly assigning an absolute magnitude within the range allowed by the spectral type bin, and then converting it to apparent magnitude. We use the same random variable to assign



absolute magnitudes within each bin for all filters, in order to keep the synthetic objects along the stellar locus in colour–colour space.

For a complete description, we also need to assign random magnitude errors to mimic an observed sample, which will depend on the particular case. Therefore, error curves as a function of magnitude for each filter are required. In Section 10.2 we detail this step for our sample. By default, *GalmodBD* accepts an exponential error distribution. In case of more sophisticated models, the error must be introduced afterwards.

For synthetic dwarfs, the code outputs its Galactic component, spectral type, Galactic coordinates ( $l, b$ ) of the centre of the pointer, distance and magnitudes in the set of filters, for example:  $i_{\text{DES}}, i_{\text{SDSS}}, z_{\text{DES}}, z_{\text{SDSS}}, Y_{\text{DES}}, J_{\text{VHS}}, J_{2\text{MASS}}, H_{\text{VHS}}, H_{2\text{MASS}}, K_{s,\text{VHS}}, K_{s,2\text{MASS}}, W1,$  and  $W2$ . Both the true and observed magnitudes, as well as their errors, are output, regardless of the chosen pair (mag, colour) used in the output expected model counts. This latter choice, coupled with the apparent magnitude range and the direction chosen, however, affects the total number of points generated.

In order to have a synthetic sample with coordinates, we randomly assign positions to the sources within the given pointer area (see Section 10.1).

These simple synthetic catalogues can be compared to a real catalogue of BD candidates by correcting the expected numbers for the visibility mask, that accounts for catalogue depth and detection variations, and for estimates of purity and completeness levels of the observed catalogue.

## 10 *GalmodBD* IN THE TARGET SAMPLE

In this section we detail the input information used to feed the *GalmodBD* simulation that reproduces the  $\text{DES} \cap \text{VHS} \cap \text{ALLWISE}$  data. Besides the empirical colour template relations, we need to define the footprint of the simulation and the photometric error model to produce realistic MLT catalogues.

### 10.1 Footprint and pointers definition

To create a sample that resembles the target sample, we create a grid of pointers following the DES tile distribution.

DES coadd data are divided into square (in spherical coordinates) regions of equal area, covering  $0.534 \text{ deg}^2$  each, called tiles. We use this information to define our pointers covering the area occupied in Fig. 1. The pointers defined to run *GalmodBD* have the same coordinates as the centre of the DES tiles and the same area of  $0.534 \text{ deg}^2$ . Later, tiles are intersected with the VHS footprint in the DES area, covering the brown areas in the same figure. Eventually, we end with 5187 pointers of  $0.534 \text{ deg}^2$ , covering  $2374 \text{ deg}^2$ .

After running the simulation in each pointer, we assign random positions within the area of the pointer to each object in the simulated catalogue. At this point we would need to consider the effect of incompleteness in the footprint, i.e. apply the footprint mask.

To study the effect the mask might have in the number of BDs recovered by our method, for each *GalmodBD* run, we create multiple synthetic position catalogues and pass the data through the footprint mask. Eventually, obtaining a statistic of the mean and standard deviation (std) of the number of MLT sources that we will lose. In our case we run 500 realizations for each *GalmodBD* model to calculate the effect on footprint completeness in Section 12.

### 10.2 Mimic DES photometric properties

Another ingredient in the *GalmodBD* simulation is the photometric errors that apply to the simulated data to create an observed synthetic sample.

To model the SNR distribution we start by selecting a random sample of the  $\text{DES} \cap \text{VHS} \cap \text{ALLWISE}$  data, limited to  $z < 23$  and selecting point sources only using the extended classification from DES Y3 data. We next apply the following algorithm for each band:

First, we divide the sample in magnitude bins of width = 0.1. For each bin, we estimate the probability density function of the magnitude error using a kernel density estimation (KDE).

With the KDE information for each thin magnitude bin, we can assign a magnitude error for a given magnitude with a dispersion that follows the KDE. Once an error is assigned to a source, we estimate apparent magnitudes assuming a Gaussian distribution centred in the true apparent magnitude and with a standard deviation equals to their magnitude error.

We extract the KDE for magnitude bins where we have more than 60 objects. In the extreme cases of very bright or very faint objects in the magnitude distribution, this requirement is not met. Therefore we expand the distribution along the bright end by repeating the KDE from the brightest bin with enough statistics. In the faint end, we fit the mean and sigma of the faintest four bins with enough statistics by a second-order polynomial and extrapolate this fit towards fainter magnitudes.

In Fig. 13 we summarize the error modelling for the bands of interest:  $i, z, Y,$  and  $J$ . In the figures, we compare the error distribution as a function of magnitude for the real data, individually for each band, with the simulated data. The median and dispersion agree very well for all bands.

## 11 *GalmodBD* RESULTS

In Table 6 we show the result of running *GalmodBD* for different galactic models varying the thin disc scale height at  $h_{z,\text{thin}} = 250, 300, 350, 400, 450, 500, 550 \text{ pc}$  and the local thick-to-thin disc density normalization  $n_{\odot,\text{thick}} = 5, 10, 15, 20$  per cent defined as  $n_{\odot,\text{thick}} = \rho_{\text{thick}}(R_{\odot})/\rho_{\text{thin}}(R_{\odot})$ . After some testing, it was clear the LT number counts were most sensitive to these two parameters. We ran the simulation for M dwarfs ranging M0 to M9 and BDs from L0 to T9 (even though the scale height of LT types does not need to be the same as for M types).

We run *GalmodBD* up to a true apparent magnitude limit of  $z_{\text{true}} < 25$ . Next, we assign errors and observed magnitudes as explained in Section 10.2. Later, we select MLT with  $z_{\text{obs}} \leq 22$  and  $(\text{SNR}) > 5\sigma$  in  $z, Y, J$  to build our simulated MLT parent catalogues. Using these catalogues, we can study the completeness and purity of our sample (see Section 12).

In Table 6, the third column is the number of M types for a given model that pass the colour cuts defined in Section 4 and  $z_{\text{obs}} < 22$  and  $(\text{SNR}) > 5\sigma$  in  $z, Y, J$ . The fourth column is the number of LT types when  $z_{\text{obs}} < 22$  and  $(\text{SNR}) > 5\sigma$  in  $z, Y, J$ . We have not applied here the colour cut, since it is a source of incompleteness and we treat it together with other effects in Section 12.

## 12 PURITY AND COMPLETENESS

In this section, we detail the various sources of error in the measurement of the number counts of LT dwarfs from the target sample. We will use a combination of both the calibration samples and the *GalmodBD* simulation. There are two issues to consider: one

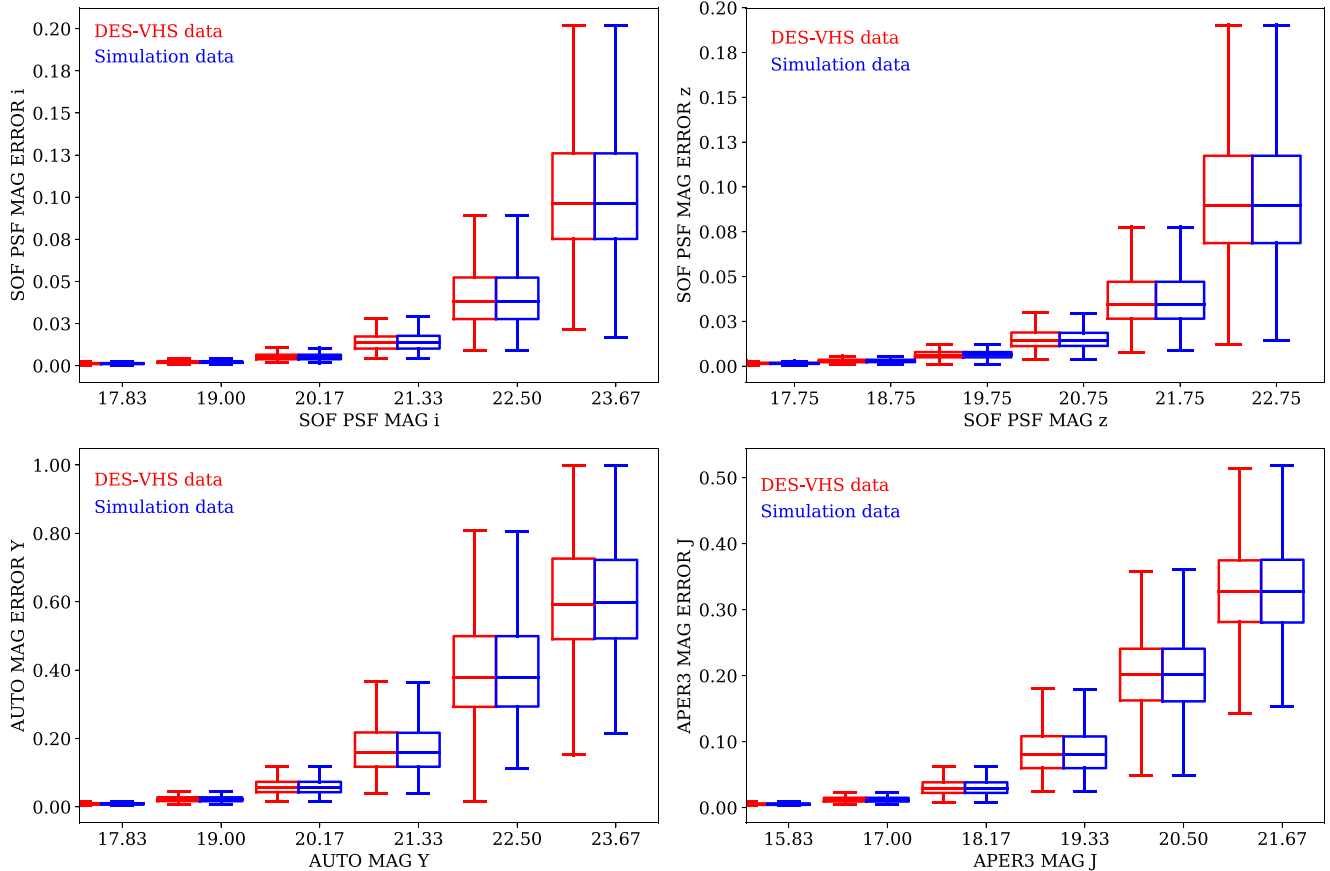


**Figure 13.** Box-plot comparing the magnitude uncertainties as a function of magnitude for DES  $i$ ,  $z$ ,  $Y$ , and VHS  $J$  data, versus the modelled distribution in *GalmodBD* simulation. In red, the DES $\cap$ VHS distribution, in blue, the simulated distribution. The horizontal line within the box indicates the median, boundaries of the box indicate the 25th- and 75th-percentile, and the whiskers indicate the highest and lowest values of the distribution. The median and dispersion agree very well for all bands.

is to identify and quantify contamination and incompleteness effects on our sample, so we can correct the simulated numbers in order to compare them to the data. The other is assessing the uncertainty associated with these corrections and the expected fluctuations in the corrected number counts. The effects we consider are as follows:

- (1) Colour–colour incompleteness: how many LT we lose by applying the colour cut to select candidates.
- (2) Loss of targets from the catalogue due to proper motions.
- (3) Footprint effects: how many LT we lose due to masking effect.
- (4) Loss of LTs due to misclassification.
- (5) Contamination of targets due to unresolved binary systems in our magnitude-limited catalogue.
- (6) Contamination by M dwarfs and extragalactic sources.

### 12.1 Incompleteness

To assess how many BDs we miss due to the colour–colour selection, we look at the number of LT types that do not enter our colour selection both in the Gagné sample as well as in the *GalmodBD* simulation. The colour range selected was chosen to minimize incompleteness. But peculiar early L dwarfs may eventually be found outside our colour range. In the Gagné sample, from the list of 104 known BDs (including young types), 2 are left outside the colour range (2 per cent). In *GalmodBD*, we have not modelled

peculiar BDs and therefore, the incompleteness level should be low. Applying the colour cut to the *GalmodBD* outputs, as expected, led to a mean completeness of 98.8 per cent. We define the colour–colour completeness correction to be the average of the two. The uncertainty associated with this correction should be low. Conservatively, we define the uncertainty to be of 1 per cent, leading to  $C_{\text{colour}} = 98.4 \pm 1$  per cent.

In order to estimate the number of missing sources due to proper motions, we will assume that the mean proper motion of LT types decreases with distance. Considering a conservative 3-yr difference in astrometry between DES and VHS, a 2 arcsec matching radius should be complete for distances  $> 50$  pc. In fact, looking at the BDs that we recover visually beyond the 2 arcsec radius in Section 3.1 and that have distances in the Gagné sample, more than 95 per cent of the missing BDs have a distance  $< 50$  pc. So we can set this as an upper limit for this effect. Above 50 pc, we match at 2 arcsec almost all of the BDs presented in the calibration sample. Likewise, we do match some of the BDs below 50 pc, at least 20 per cent of them.

In summary, matching the Gagné sample to DES within 2 arcsec we recover 20 per cent of the BDs below 50 pc and 100 per cent above that distance. This is a conservative limit, but it gives us a sense of the percentage loose by proper motions. Note that we have not considered here that we might miss some of the targets due to the incompleteness of the footprint so the 20 per cent should be higher.

If we now look at the *GalmodBD* simulation, we predict the number of LT types with distances  $< 50$  pc to be 2 per cent of the whole sample. Considering an 80 per cent completeness and an error in the determination comparable to the effect itself, it results in a proper motion completeness correction of  $C_{pm} = 98.4 \pm 2$  per cent.

In terms of footprint incompleteness, we apply the algorithm presented in Section 10.1 to estimate the effect of the footprint mask: we produce 500 realizations of each *GalmodBD* model and estimate the mean and std of LT type number counts that survive the masking process. We then average over all models to obtain a model-independent completeness correction of  $C_{foot} = 93.6 \pm 3.5$  per cent.

Finally, there is the effect of misclassification of LT types as M types. We estimated the incompleteness of LT types due to misclassification as  $C_{classif} = 85 \pm 1$  per cent. In the next subsection, we describe this correction along with the corresponding contamination effect, namely the misclassification of M dwarfs as LT types.

## 12.2 Contamination

Our LT dwarfs catalogue is limited to  $z \leq 22$ . Unresolved binary systems containing two LT dwarfs will have a higher flux than a single object and hence will make into the catalogue even though each member of the system individually would not. This boosts the total number of LTs in our sample. We estimate the effect of unresolved binarism systems as follows. According to Luhman (2012) (and references therein), the fraction of binaries decreases with the mass of the primary, while the mass ratio ( $q = m_1/m_2$ ) tends to unity (equal-mass binaries). In our case, we are only interested in those binaries where the primary is an LT. Binary systems with the LT as secondary, will have a small mass ratio ( $q \ll 1$ ), and therefore, they will be uncommon. Also, we cannot census this type of population since the light from the primary will dominate the light from secondary. Luhman (2012) quotes different estimates the fraction of binaries where the primary is an LT,  $f_{bin}$ . Observational data suggest  $f_{bin} \simeq 7$  per cent, but may be prone to incompleteness, especially for close pairs. Theoretical models of BD formation predict  $f_{bin}$  in the 20–30 per cent range (Maxted & Jeffries 2005; Basri & Reiners 2006). None the less, a recent estimate by Fontanive et al. (2018) would confirm the empirical trend of Luhman (2012) and therefore we here adopt  $f_{bin} = 0.07$ . If we assume that  $q \sim 1$  in all cases, we will obtain binary systems that have the same spectral type as the primary, but with a magnitude that is 0.75 times brighter (since the system flux is twice that of the primary). To estimate the contamination by binaries in the target sample, we follow the description of Burningham et al. (2010). According to equation 3 in that paper, the correction factor is

$$P_{binary} = \frac{\gamma - 1}{\gamma + 1/f_{bin} - 1}, \quad (5)$$

where  $\gamma = 2\sqrt{2}$  for equal mass/luminosity binaries, and  $f_{bin} = 0.07$ . Finally, we get  $P_{binary} = 11 \pm 1$  per cent.

There are two additional sources of contaminants applied here: one is the migration of M dwarfs that have been wrongly assigned as LT type after running *classif*, and the other is the contamination by extragalactic sources.

Ideally, in order to estimate the contamination by M dwarfs and the incompleteness of LT types due to the photometric classification, we should run *classif* on the output of *GalmodBD*. Unfortunately, our classification code is fed with the same templates used in the simulation and, therefore, the classification uncertainty we get by

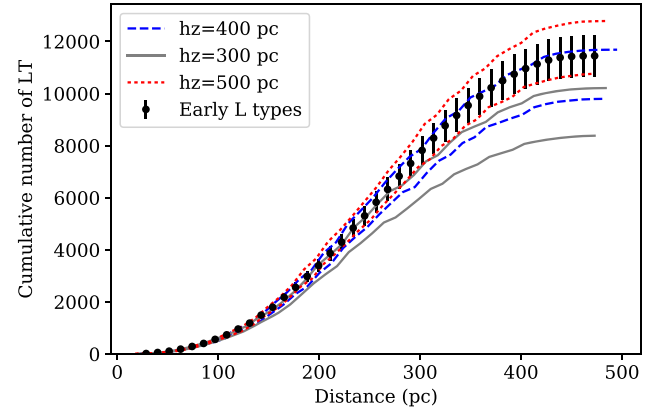


**Figure 14.** Comparison of the number counts of early L types (L0–L3) with three models of the thin disc scale height. In grey we show models with a scale height similar to that for M dwarfs (Jurić et al. 2008) with  $h_z^{thin} = 300$  pc, in dashed blue, models with  $h_z^{thin} = 400$  pc and in red, models with  $h_z^{thin} = 500$  pc. For each model we show two estimates, one where  $n_{\odot,thick} = 5$  per cent (lower limit) and another where  $n_{\odot,thick} = 20$  per cent (upper limit).

running *classif* in *GalmodBD* is unrealistically low. In order to estimate the number of M dwarfs that are classified as LT types and vice versa, we perturb the true spectral types for *GalmodBD* sources following a normal distribution with dispersion given in Section 5.1:  $\sigma_M = 0.69$ ,  $\sigma_L = 1.03$ , and  $\sigma_T = 1.12$  and mean value centred in the true spectral type.

Once we perturb the true spectral types to get a pseudo-photometric calibration in *GalmodBD*, we can estimate how many LTs will be classified as M, and vice versa. We estimate this number for all the *GalmodBD* realizations and find that  $\sim 11$  per cent of M dwarfs (after the colour cut) are given LT type. This corresponds to contamination by about 14–19 per cent of the corresponding LT simulated sample. This means a mean LT purity level of  $P_{class} = 83 \pm 2$  per cent. We also use the same procedure applied on the *GalmodBD* data to assess the number of LT types migrating to M type. This is an additional incompleteness of  $C_{class} = 85 \pm 1$  per cent, to be added to those from the previous subsection.

The removal of extragalactic contaminants is another source of uncertainty. We saw in Section 6 that  $\lesssim 10$  per cent of the MLT sample have galaxy or quasar class. These are not modelled in *GalmodBD*, and therefore we do not need to apply a correction due to extragalactic contamination, although there will always be uncertainty associated with it. Based on tests with different LEPHARE SED libraries and the ambiguity in classification for sources with  $NBANDS < 5$ , we estimate a standard deviation associated with the removal of extragalactic sources of  $\sigma_{SG} \sim 5$ . per cent.

## 12.3 Completeness and purity summary

Summarizing all these effects, we estimate the completeness and contamination up to  $z < 22$  at  $5\sigma$  as follows:

- (1) Completeness due to the colour–colour cut of  $C_{colour} = 98.4 \pm 1$ . per cent.
- (2) Completeness due to proper motions of  $C_{pm} = 98.4 \pm 2$  per cent.
- (3) Completeness due to masking of  $C_{foot} = 93.6 \pm 3.5$  per cent.

(4) Completeness due to LT misclassified as M types of  $C_{\text{class}} = 85 \pm 1$  per cent.

(5) Contamination due to unresolved binary systems measured as the fraction  $f_{\text{bin}} = 7$  per cent of sources:  $K_{\text{bin}} = 11 \pm 1$  per cent.

(6) Contamination of the LT sample due to M types classified as LTs:  $K_{\text{class}} = 17 \pm 2$  per cent.

(7) Uncertainty in the extragalactic contamination removal algorithm introduces an additional systematic error of  $\sigma_{\text{extra}} = 5$  per cent.

Combining all these effects, we define a correction factor:

$$CP_{\text{LT}} = \frac{C_{\text{colour}} \times C_{\text{pm}} \times C_{\text{foot}} \times C_{\text{class}}}{(1 - K_{\text{bin}}) \times (1 - K_{\text{class}})} \quad (6)$$

that multiplies the LT sample. This correction factor accounts for the effect of incompleteness and purity, and applies to our definition with  $z < 22$  and  $5\sigma$  in  $z, Y, J$ . Different magnitude limits would lead to different corrections. In this case, the final correction factor is  $C_{\text{LT}} = 1.05$ . This factor is applied to the number of detected LT  $N(\text{LT})_{\text{obs}} = 11\,745$  to get an estimate of the total number of LT in the footprint up to  $z < 22$  with at least a  $5\sigma$  detection in  $z, Y, J$  as  $N(\text{LT})_{\text{true}} = N(\text{LT})_{\text{obs}} \times C_{\text{LT}}$ . At first approximation, the uncertainty in the number of LT types is the square root of the sum of the squares of the individual errors listed above:

$$\sigma_{\text{LT}} = \sqrt{\sigma_{\text{col}}^2 + \sigma_{\text{pm}}^2 + \sigma_{\text{bin}}^2 + \sigma_{\text{foot}}^2 + \sigma_{\text{cl,C}}^2 + \sigma_{\text{cl,P}}^2 + \sigma_{\text{ex}}^2} \quad (7)$$

with  $\sigma_{\text{LT}} \sim 7$  per cent. Finally, the number of LT's to compare against different Milky Way models is in round numbers  $N(\text{LT}) \sim 12\,300 \pm 900$ . If we only select the early L types (L0–L3) for which we want to estimate the thin disc scale height, the number to compare with becomes  $N(L_{0,1,2,3}) \sim 11\,500 \pm 800$ .

### 13 THE THIN DISC SCALE HEIGHT

Jurić et al. (2008) estimate the thin disc scale height and the local thick-to-thin disc density normalization of SDSS M dwarfs up to a distance of 2 kpc. They found  $h_{z,\text{thin}} = 300$  pc and  $n_{\odot,\text{thick}} = 12$  per cent.

As a first application of the BD catalogue and *GalmodBD*, we compare the number of observed LT types with different realizations of *GalmodBD* to shed light on the thin disc scale height of the LT population. Since T types are less than 2 per cent of the sample and go only up to 100 pc, in practice, we are estimating the scale height of the early L types (L0–L3). A previous attempt to measure the thin disc scale height of L types can be found in Ryan et al. (2005), where they estimate a value of  $h_{z,\text{thin}} = 350 \pm 50$  using only 28 LT types and on a very simplistic Galactic model. Since our model is more detailed and we have a much higher statistic, we believe that our results will be more reliable. More recently, Sorahana et al. (2018) have used data from the first data release from the HSC (Aihara et al. 2018; Miyazaki et al. 2018) to estimate the vertical thin disc scale height of early L types with an estimate between 320 and 520 pc at 90 per cent confidence.

Comparing the value of  $N(\text{LT}) \sim 12000 \pm 900$  with the grid of *GalmodBD* (Table 8), we do find a higher scale height than that of M dwarfs, as Ryan et al. (2005) found, of the order of  $h_{z,\text{thin}} \sim 450$  pc. None the less, there is a degeneracy between the thin disc scale height and  $n_{\odot,\text{thick}}$  and therefore we cannot yet rule out a models with  $h_{z,\text{thin}} = 300$  pc: considering the error in the number counts  $\sigma_{\text{LT}} \sim 900$ , there are models of  $h_{z,\text{thin}} = 300$  pc which predicts a number of LT types within  $1\sigma$  of our measurement. In Fig. 14 we compare the

number counts to various models taken from *GalmodBD*. In grey we show two models for  $h_{z,\text{thin}} = 300$  pc, one with  $n_{\odot,\text{thick}} = 5$  per cent (lower limit) and another with  $n_{\odot,\text{thick}} = 20$  per cent (upper limit). In dashed blue we show models for  $h_{z,\text{thin}} = 400$  pc, for same values of  $n_{\odot,\text{thick}}$  and in red points we show models for  $h_{z,\text{thin}} = 500$  pc.

The estimated scale height for the sample of substellar candidate sources is larger than typical values of main sequence stars of GK types, usually in the range 300–350 pc. In a stellar system where all stellar and substellar objects form from a dynamically cold rotating gas settled close to the disc mid-plane and are gradually perturbed by dynamical interactions with gas clouds and spiral arms, a higher scale height is interpreted as an indication of an older age. In fact, we may attempt to convert our best estimate of  $h_z^{\text{thin}} = 450$  pc into a vertical velocity dispersion, following a similar procedure to Ryan et al. (2017). But in our case we adopt the  $n = \infty$  model by van der Kruit (1988), which corresponds to an exponential density law perpendicular to the disc plane. We adopt the same value for the total surface density of matter responsible for the gravitational field, namely  $\sigma = 68 M_{\odot} \text{pc}^2$  (Bovy & Rix 2013), to yield a velocity dispersion  $\sigma_z \simeq 26 \text{ km s}^{-1}$  at  $z = h_z^{\text{thin}}$  and  $\sigma_z \simeq 20 \text{ km s}^{-1}$  at  $z = 0$  (mid-plane). We note that this vertical dispersion velocity is larger than those quoted by Burgasser et al. (2015) for M dwarfs. A  $h_z^{\text{thin}} \simeq 300$  pc, which is not consistent with our results for the early L types (L0–L3) dwarfs, would be required to match their M dwarfs kinematics perpendicular to the disc plane. Our results also seem to indicate a kinetically hotter population than the L dwarfs by those same authors, especially when compared to their core (dynamically colder) sample. This may indicate that we are sampling an older L dwarfs at typically larger distances from the disc plane than typical spectroscopic samples.

In order to properly constrain the thin disc scale height in the future, we will perform a Markov chain Monte Carlo analysis which will marginalize over  $n_{\odot,\text{thick}}$ . This will be the scope of a future analysis. We will wait until the full coverage of DES and VHS have been achieved, covering  $\sim 5000 \text{ deg}^2$ . Here we will apply the same methodology presented here, for magnitudes  $z < 22.7$ , increasing both the area and the distance of the surveyed sample.

### 14 CONCLUSION

In this paper, we apply a photometric BD classification scheme based on Skrzypek et al. (2015) to  $\text{DES} \cap \text{VHS} \cap \text{AllWISE}$  data using eight bands covering a wavelength range between 0.7 and 4.6  $\mu\text{m}$ . Since several degeneracies are found in colour space between spectral types M, L, and T, the use of multiple bands are required for a good spectral type calibration.

In comparison with Skrzypek et al. (2015), we can go to greater distances in the L regime due to the deeper DES and VHS samples, in contrast with the SDSS  $\cap$  UKIDSS design. This way, we classify 11 745 BDs in the spectral regime from L0 to T9 in  $\approx 2400 \text{ deg}^2$ , with a similar spectral resolution of one spectral type. We make this catalogue public in electronic format. It can be downloaded from <https://des.ncsa.illinois.edu/releases/other/y3-mlt>. This is the largest LT sample ever published. We further estimate the purity and completeness of the sample. We estimate the sample to be  $\sim 77$  per cent complete and  $\sim 74$  per cent pure at  $z_{\text{AB}} < 22$ . Finally, we can calculate the total number of LTs in the DES  $\cap$  VHS footprint to be  $\sim 12\,300 \pm 900$ .

During the classification, we identify 2818 possible extragalactic sources that we removed from the catalogue, containing 57 quasars at high redshift. The removal of extragalactic sources increases the uncertainty in the determination of the number of LT types.



In parallel, we have presented the *GalmodBD* simulation, a simulation that computes LT number counts as a function of SFH parameters. In our analysis, we found that the thin disc scale height and the thin-to-thick disc normalization were the parameters that most affect the number counts. None the less, more free parameters are available in the simulation. When comparing the simulation output with the number of LT expected in the footprint, we put constraints on the thin disc scale height for early L types (L0–L3), finding a value that is in agreement with recent measurements, like the one found in Sorahana et al. (2018) with  $h_z^{\text{thin}} \sim 400$  pc.

Having these two ingredients, a robust simulation of number counts, and a methodology to select BDs in  $\text{DES} \cap \text{VHS} \cap \text{AI}/\text{WISE}$  will allow us to do a precise measurement of the thin disc scale height of the L population, putting BD science in its Galactic context. This will be the scope of future analyses.

## ACKNOWLEDGEMENTS

Funding for the DES Projects has been provided by the U.S. Department of Energy, the U.S. National Science Foundation, the Ministry of Science and Education of Spain, the Science and Technology Facilities Council of the United Kingdom, the Higher Education Funding Council for England, the National Center for Supercomputing Applications at the University of Illinois at Urbana-Champaign, the Kavli Institute of Cosmological Physics at the University of Chicago, the Center for Cosmology and Astro-Particle Physics at the Ohio State University, the Mitchell Institute for Fundamental Physics and Astronomy at Texas A&M University, Financiadora de Estudos e Projetos, Fundação Carlos Chagas Filho de Amparo à Pesquisa do Estado do Rio de Janeiro, Conselho Nacional de Desenvolvimento Científico e Tecnológico and the Ministério da Ciência, Tecnologia e Inovação, the Deutsche Forschungsgemeinschaft, and the Collaborating Institutions in the Dark Energy Survey.

The Collaborating Institutions are Argonne National Laboratory, the University of California at Santa Cruz, the University of Cambridge, Centro de Investigaciones Energéticas, Medioambientales y Tecnológicas-Madrid, the University of Chicago, University College London, the DES-Brazil Consortium, the University of Edinburgh, the Eidgenössische Technische Hochschule (ETH) Zürich, Fermi National Accelerator Laboratory, the University of Illinois at Urbana-Champaign, the Institut de Ciències de l’Espai (IEEC/CSIC), the Institut de Física d’Altes Energies, Lawrence Berkeley National Laboratory, the Ludwig-Maximilians Universität München and the associated Excellence Cluster Universe, the University of Michigan, the National Optical Astronomy Observatory, the University of Nottingham, The Ohio State University, the University of Pennsylvania, the University of Portsmouth, SLAC National Accelerator Laboratory, Stanford University, the University of Sussex, Texas A&M University, and the OzDES Membership Consortium.

Based in part on observations at Cerro Tololo Inter-American Observatory, National Optical Astronomy Observatory, which is operated by the Association of Universities for Research in Astronomy (AURA) under a cooperative agreement with the National Science Foundation.

The DES data management system is supported by the National Science Foundation under Grant Numbers AST-1138766 and AST-1536171. The DES participants from Spanish institutions are partially supported by MINECO under grants AYA2015-71825, ESP2015-66861, FPA2015-68048, SEV-2016-0588, SEV-2016-0597, and MDM-2015-0509, some of which include ERDF funds from the European Union. IFAE is partially funded by the

CERCA program of the Generalitat de Catalunya. Research leading to these results has received funding from the European Research Council under the European Union’s Seventh Framework Program (FP7/2007-2013) including ERC grant agreements 240672, 291329, and 306478. We acknowledge support from the Australian Research Council Centre of Excellence for All-sky Astrophysics (CAASTRO), through project number CE110001020, and the Brazilian Instituto Nacional de Ciência e Tecnologia (INCT) e-Universe (CNPq grant 465376/2014-2).

This manuscript has been authored by Fermi Research Alliance, LLC under Contract No. DE-AC02-07CH11359 with the U.S. Department of Energy, Office of Science, Office of High Energy Physics. The United States Government retains and the publisher, by accepting the article for publication, acknowledges that the United States Government retains a non-exclusive, paid-up, irrevocable, world-wide license to publish or reproduce the published form of this manuscript, or allow others to do so, for United States Government purposes.

This publication makes use of data products from the Vista Hemisphere Survey based on observations made with ESO Telescopes at the La Silla or Paranal Observatories under programme ID(s) 179.A-2010(A), 179.A-2010(B), 179.A-2010(C), 179.A-2010(D), 179.A-2010(E), 179.A-2010(F), 179.A-2010(G), 179.A-2010(H), 179.A-2010(I), 179.A-2010(J), 179.A-2010(K), 179.A-2010(L), 179.A-2010(M).

This publication makes use of data products from the Wide-field Infrared Survey Explorer, which is a joint project of the University of California, Los Angeles, and the Jet Propulsion Laboratory/California Institute of Technology, and NEOWISE, which is a project of the Jet Propulsion Laboratory/California Institute of Technology. WISE and NEOWISE are funded by the National Aeronautics and Space Administration.

This paper has gone through internal review by the DES collaboration. We also thanks the anonymous referee from MNRAS for their useful comments.

ACR acknowledges financial support provided by the PAPDRJ CAPES/FAPERJ Fellowship and by ‘Unidad de Excelencia María de Maeztu de CIEMAT – Física de Partículas (Proyecto MDM)’.

The authors would like to thank Jacqueline Faherty and Joe Filippazzo for their help on the early stages of this project.

## REFERENCES

- Abell P. A. et al., 2009, LSST Science Book v2.0 ([arXiv:0912.0201](https://arxiv.org/abs/0912.0201))  
 Aihara H. et al., 2018, *PASJ*, 70  
 Albert L., Artigau É., Delorme P., Reyly C., Forveille T., Delfosse X., Willott C. J., 2011, *AJ*, 141, 203  
 An D. et al., 2008, *ApJS*, 179, 326  
 Arnouts S., Cristiani S., Moscardini L., Matarrese S., Lucchin F., Fontana A., Giallongo E., 1999, *MNRAS*, 310, 540  
 Arnouts S. et al., 2007, *A&A*, 476, 137  
 Banerji M. et al., 2015, *MNRAS*, 446, 2523  
 Basri G., Reiners A., 2006, *AJ*, 132, 663  
 Bennett M., Bovy J., 2019, *MNRAS*, 482, 1417  
 Bertin E., Arnouts S., 1996, *A&AS*, 117, 393  
 Bochanski J. J., Munn J. A., Hawley S. L., West A. A., Covey K. R., Schneider D. P., 2007, *AJ*, 134, 2418  
 Bovy J., Rix H.-W., 2013, *ApJ*, 779, 115  
 Bruzual G., Charlot S., 2003, *MNRAS*, 344, 1000  
 Burgasser A. J., 2007, *ApJ*, 659, 655  
 Burgasser A. J. et al., 2003, *ApJ*, 592, 1186  
 Burgasser A. J., Kirkpatrick J. D., Cruz K. L., Reid I. N., Leggett S. K., Liebert J., Burrows A., Brown M. E., 2006a, *ApJS*, 166, 585  
 Burgasser A. J., Geballe T. R., Leggett S. K., Kirkpatrick J. D., Golimowski D. A., 2006b, *ApJ*, 637, 1067

- Burgasser A. J. et al., 2015, *AJ*, 149, 104
- Burke D. L. et al., 2018, *AJ*, 155, 41
- Burningham B., 2018, *Handbook of Exoplanets*, ISBN 978-3-319-55332-0. Springer International Publishing AG, part of Springer Nature, p. 118
- Burningham B. et al., 2010, *MNRAS*, 406, 1885
- Burningham B. et al., 2013, *MNRAS*, 433, 457
- Burstein D., Heiles C., 1982, *AJ*, 87, 1165
- Chiu K., Fan X., Leggett S. K., Golimowski D. A., Zheng W., Geballe T. R., Schneider D. P., Brinkmann J., 2006, *AJ*, 131, 2722
- Coleman G. D., Wu C.-C., Weedman D. W., 1980, *ApJS*, 43, 393
- Cross N. J. G. et al., 2012, *A&A*, 548, A119
- Cruz K. L. et al., 2007, *AJ*, 133, 439
- Dalton G. B. et al., 2006, in McLean I. S., Iye M., eds, *Proc. SPIE Conf. Ser. Vol. 6269, Ground-based and Airborne Instrumentation for Astronomy*. SPIE, Bellingham, p. 62690X
- Dark Energy Survey Collaboration, 2016, *MNRAS*, 460, 1270
- Dark Energy Survey Collaboration, 2018, *ApJS*, 239, 18
- Day-Jones A. C. et al., 2013, *MNRAS*, 430, 1171
- Drlica-Wagner A. et al., 2018, *ApJS*, 235, 33
- Dupuy T. J., Liu M. C., 2012, *ApJS*, 201, 19
- Faherty J. K., Burgasser A. J., Cruz K. L., Shara M. M., Walter F. M., Gelino C. R., 2009, *AJ*, 137, 1
- Faherty J. K. et al., 2012, *ApJ*, 752, 56
- Faherty J. K. et al., 2016, *ApJS*, 225, 10
- Filippazzo J. C., Rice E. L., Faherty J., Cruz K. L., Van Gordon M. M.,Looper D. L., 2015, *ApJ*, 810, 158
- Folkes S. L., Pinfield D. J., Kendall T. R., Jones H. R. A., 2007, *MNRAS*, 378, 901
- Fontanive C., Biller B., Bonavita M., Allers K., 2018, *MNRAS*, 479, 2702
- Gagné J. et al., 2017, *ApJS*, 228, 18
- Gaia Collaboration, 2018, *A&A*, 616, A1
- Ilbert O. et al., 2006, *A&A*, 457, 841
- Jurić M. et al., 2008, *ApJ*, 673, 864
- Kerber L. O., Javiel S. C., Santiago B. X., 2001, *A&A*, 365, 424
- Kinney A. L., Calzetti D., Bohlin R. C., McQuade K., Storchi-Bergmann T., Schmitt H. R., 1996, *ApJ*, 467, 38
- Kirkpatrick J. D. et al., 1999, *ApJ*, 519, 802
- Kirkpatrick J. D. et al., 2011, *ApJS*, 197, 19
- Lawrence A. et al., 2007, *MNRAS*, 379, 1599
- Leggett S. K., Morley C. V., Marley M. S., Saumon D., Fortney J. J., Visscher C., 2013, *ApJ*, 763, 130
- Leggett S. K., Morley C. V., Marley M. S., Saumon D., 2015, *ApJ*, 799, 37
- Liu M. C. et al., 2013, *ApJ*, 777, L20
- Lodieu N. et al., 2012, *A&A*, 548, A53
- Looper D. L. et al., 2008, *ApJ*, 686, 528
- Luhman K. L., 2012, *ARA&A*, 50, 65
- Mainzer A. et al., 2011, *ApJ*, 731, 53
- Marocco F. et al., 2014, *MNRAS*, 439, 372
- Marocco F. et al., 2015, *MNRAS*, 449, 3651
- Marocco F. et al., 2017, *MNRAS*, 470, 4885
- Maxted P. F. L., Jeffries R. D., 2005, *MNRAS*, 362, L45
- McMahon R. G., Banerji M., Gonzalez E., Koposov S. E., Bejar V. J., Lodieu N., Rebolo R., VHS Collaboration, 2013, *The Messenger*, 154, 35
- Miyazaki S. et al., 2018, *PASJ*, 70, S1
- Morganson E. et al., 2018, *PASP*, 130, 074501
- Pinfield D. J., Jones H. R. A., Lucas P. W., Kendall T. R., Folkes S. L., Day-Jones A. C., Chappelle R. J., Steele I. A., 2006, *MNRAS*, 368, 1281
- Prevot M. L., Lequeux J., Maurice E., Prevot L., Rocca-Volmerange B., 1984, *A&A*, 132, 389
- Reed S. L. et al., 2015, *MNRAS*, 454, 3952
- Reed S. L. et al., 2017, *MNRAS*, 468, 4702
- Ryan R. E., Jr, Hathi N. P., Cohen S. H., Windhorst R. A., 2005, *ApJ*, 631, L159
- Ryan Russell E. J. et al., 2017, *ApJ*, 847, 53
- Santiago B. X., Gilmore G., Elson R. A. W., 1996, *MNRAS*, 281, 871
- Santiago B., Yanny B., 2010, in Bruzual G. R., Charlot S., eds, *Stellar Populations – Planning for the Next Decade*. Proceedings of the International Astronomical Union., IAU Symposium, Volume 262. Cambridge University Press, United Kingdom, p. 265
- Schlafly E. F., Finkbeiner D. P., 2011, *ApJ*, 737, 103
- Schlegel D. J., Finkbeiner D. P., Davis M., 1998, *ApJ*, 500, 525
- Schmidt S. J., West A. A., Hawley S. L., Pineda J. S., 2010, *AJ*, 139, 1808
- Skemer A. J. et al., 2016, *ApJ*, 826, L17
- Skrzypczek N., Warren S. J., Faherty J. K., Mortlock D. J., Burgasser A. J., Hewett P. C., 2015, *A&A*, 574, A78
- Skrzypczek N., Warren S. J., Faherty J. K., 2016, *A&A*, 589, A49
- Smith L., Lucas P. W., Burningham B., Jones H. R. A., Smart R. L., Andrei A. H., Catalán S., Pinfield D. J., 2014, *MNRAS*, 437, 3603
- Sorahana S., Nakajima T., 2019, *AJ*, 870, 118
- Tie S. S. et al., 2017, *AJ*, 153, 107
- van der Kruit P. C., 1988, *A&A*, 192, 117
- Warren S. J. et al., 2007, *MNRAS*, 379, 1599
- West A. A. et al., 2011, *AJ*, 141, 97
- Wright E. L. et al., 2010, *AJ*, 140, 1868
- Zhang Z. H., Homeier D., Pinfield D. J., Lodieu N., Jones H. R. A., Allard F., Pavlenko Y. V., 2017, *MNRAS*, 468, 261

## SUPPORTING INFORMATION

Supplementary data are available at *MNRAS* online.

### DES Y3 LT catalog.fits

### DES Y3 M catalog.fits

Please note: Oxford University Press is not responsible for the content or functionality of any supporting materials supplied by the authors. Any queries (other than missing material) should be directed to the corresponding author for the article.

## APPENDIX A: LEPHARE CONFIGURATION

In this section, we detail the LEPHARE configuration we used to separate extragalactic sources from the main MLT catalogue. We run separately LEPHARE for galaxy and quasar templates.

We used AVEROIN galaxy template library, containing 62 different templates including starburst, spiral, elliptical, and irregular galaxies from Coleman, Wu & Weedman (1980), Kinney et al. (1996), and Bruzual & Charlot (2003) and tuned in the mid-infrared (from 3.6 to 4.5  $\mu\text{m}$ ) based on VVDS-CFHTLS-SWIRE photometry and VVDS spectra. They were used for the first in Arnouts et al. (2007). We allow for internal extinction following the extinction law by Prevot et al. (1984) up to a  $E(B - V) = 0.3$ . In Table A1 we summarize the configuration parameters we used in LEPHARE.

For quasars, we use the default quasar template list from LEPHARE and we refer to their documentation for details about the templates used. In Table A2 we summarize the configuration used for the quasar run.

We further need the filter passbands for  $i$ ,  $z$ ,  $Y$  (DES),  $J$ ,  $H$ ,  $K_s$  (VHS), and  $W1$ ,  $W2$  (WISE). The DES passbands are the most updated versions of the calibrated transmission curves as shown in Burke et al. (2018), for the VHS passbands, we use the curves given at ESO instrument description page<sup>9</sup> while for the WISE filters we used the curves given at the WISE documentation page.<sup>10</sup>

Finally, we add an error of 0.07 in quadrature to each magnitude error as we did for the main *classify* run and transform magnitudes to AB previous to run LEPHARE.

<sup>9</sup><http://www.eso.org/sci/facilities/paranal/instruments/vircam/inst.html>

<sup>10</sup><http://www.astro.ucla.edu/wright/WISE/passbands.html>

**Table A1.** LEPHARE configuration used when fitting the data to galaxy templates.

Name	Value	Explanation
GAL_SED	AVEROIN_MOD.list	List of 62 galaxy templates
GAL_FSCALE	1.	Arbitrary Flux Scale
FILTER_LIST	$i, z, Y, J, H, K_s, W1, W2$	List of paths to ascii files with passbands
TRANS_TYPE	0	Transmission type (0 = Energy, 1 = Nb of photons)
FILTER_CALIB	0	Filter calibration (0 = $f_{nu} = ctt$ )
MAGTYPE	AB	Magnitude type (AB or VEGA)
Z_STEP	0.04, 6., 0.1	$dz, z_{max}, dz_{sup}$
COSMOLOGY	70, 0.3, 0.7	$H_0, \Omega_M, \Omega_\Lambda$
EXTINC_LAW	SMC_prevot.dat	Extinction law
EB_V	0., 0.05, 0.1, 0.15, 0.2, 0.3	Allowed $E(B - V)$ values
MOD_EXTINC	38, 62	Templates for which to apply extinction law
EM_LINES	NO	Allow emission lines
CAT_MAG	AB	Input magnitude (AB or VEGA)
ERR_SCALE	0.07	Errors per band added in quadrature
Z_INTERP	YES	Redshift interpolation

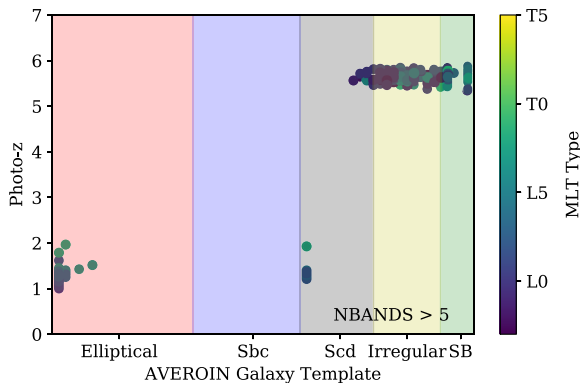
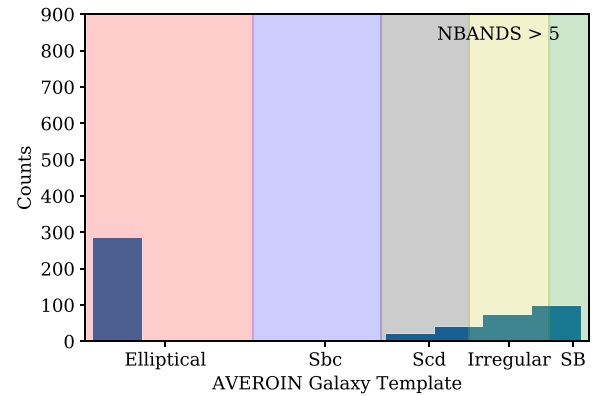
**Table A2.** LEPHARE configuration used to fit the data to quasar templates.

Name	Value	Explanation
GAL_SED	QSO_MOD.list	List of 28 quasar templates
GAL_FSCALE	1.	Arbitrary Flux Scale
FILTER_LIST	$i, z, Y, J, H, K_s, W1, W2$	List of paths to ascii files with passbands
TRANS_TYPE	0	Transmission type (0 = Energy, 1 = Nb of photons)
FILTER_CALIB	0	Filter calibration (0 = $f_{nu} = ctt$ )
MAGTYPE	AB	Magnitude type (AB or VEGA)
Z_STEP	0.04, 9., 0.1	$dz, z_{max}, dz_{sup}$
COSMOLOGY	70, 0.3, 0.7	$H_0, \Omega_M, \Omega_\Lambda$
EB_V	None	Allowed $E(B - V)$ values
CAT_MAG	AB	Input magnitude (AB or VEGA)
ERR_SCALE	0.07	Errors per band added in quadrature
Z_INTERP	YES	Redshift interpolation

## APPENDIX B: GALAXY CONTAMINATION IN THE MLT CATALOGUE

In this section we describe the extragalactic population found in the colour space defined in Section 4 after running LEPHARE. From the list of 2818 targets, 2761 are galaxies, and 57 are quasars. Next, we show the properties of the galaxy population.

To avoid biases in our conclusions due to a wrong classification as explained in Section 6.1, we analyse only sources with  $NBANDS > 5$ . From the list of 2761 extragalactic sources, 514 targets meet

**Figure B1.** Best galaxy templates versus redshift for extragalactic targets with  $NBANDS > 5$ . The colour scale is given by the colour bar and represent the best-fitting MLT type.**Figure B2.** Best galaxy template distribution for extragalactic targets with  $NBANDS > 5$ .

this requirement. In this sample, we identify two phenotypes of galaxies that mimic the LT colours: elliptical galaxies at redshifts  $1 < z < 2$ , and another phenotype of spirals and irregulars with  $5 < z < 6$ . In Fig. B1 we show the best-fitting galaxy template versus the redshift. In colour scale, the best-fitting MLT type is presented. In Fig. B2 we show the number of extragalactic sources as a function of galaxy spectral type. The contamination happens only in the ML regime.

**Table C1.** The MW model adopted in this work. The columns list: the formula for each MW component (first), free parameters for each component (second), meaning of the parameter (third), units (forth column), value (fifth column), and if the parameter is fixed or varied in the current analysis (last column). The MW model is described by exponential laws to the thin and thick disc and by a de-projected de Vaucouleurs profile to the Halo.

Formula	Symbol	Meaning	Unit	Value	Fixed/varied
<b>Thin disc</b>					
$\rho^{\text{thin}} = \rho_{\odot}^{\text{thin}} \exp[-( z  -  z_{\odot} )/h_z^{\text{thin}}] \times \exp(-(R - R_{\odot})/h_R^{\text{thin}})$ for $(R < R_{\text{max}}^{\text{thin}})$ with $\rho^{\text{thin}}(R_{\odot}, 0, z_{\odot}) = \rho_{\odot}^{\text{thin}}$	$h_R^{\text{thin}}$	Thin disc scale length	kpc	2.5	Fixed
	$R_{\text{max}}^{\text{thin}}$	Maximum radius	kpc	25	Fixed
	$h_z^{\text{thin}}$	Thin disc scale height	pc	Table 6, col. 1	Varied
	$\rho_{\odot}^{\text{thin}}$	Local thin disc density	pc <sup>-3</sup>	Section 8.1	Fixed
<b>Thick disc</b>					
$\rho^{\text{thick}} = n_{\odot, \text{thick}} \rho_{\odot}^{\text{thin}} \exp[-( z  -  z_{\odot} )/h_z^{\text{thick}}] \times \exp(-(R - R_{\odot})/h_R^{\text{thick}})$ for $(R < R_{\text{max}}^{\text{thick}})$	$h_z^{\text{thick}}$	Thick disc scale height	kpc	1.0	Fixed
	$h_R^{\text{thick}}$	Thick disc scale length	kpc	2.5	Fixed
	$n_{\odot, \text{thick}}$	Local thick/thin disc Normalization	–	Table 6, col. 2	Varied
	$R_{\text{max}}^{\text{thick}}$	Maximum radius	kpc	25	Fixed
<b>Halo</b>					
$\rho^{\text{halo}} = \rho_{\odot}^{\text{halo}} \left( \frac{r_q^{-7/8} \exp[-7.67(r_q/r_e)^{1/4}]}{r_{\odot}^{-7/8} \exp[-7.67(r_{\odot}/r_e)^{1/4}]} \right)$ with $r_q = \sqrt{(R^2 + (z/q)^2)q}$ with $\rho^{\text{halo}}(R_{\odot}, 0, z_{\odot}) = \rho_{\odot}^{\text{halo}}$	$r_e$	Half-light radius	kpc	3.0	Fixed
	$q$	Oblate axial ratio $z/x$	–	0.800	Fixed
	$\rho_{\odot}^{\text{halo}}$	Local halo density	pc <sup>-3</sup>	$0.003 \times \rho_{\odot}^{\text{thin}}$	Fixed
<b>Others</b>					
	$R_{\odot}$	Sun's distance to the GC	kpc	8.0	Fixed
	$z_{\odot}$	Sun's height above the plane	pc	20.8 <sup>a</sup>	Fixed

<sup>a</sup>Bennett & Bovy (2019).

## APPENDIX C: DENSITY EQUATIONS

Table C1 summarizes the functional form utilized for each Galactic component, the parameters that describe the component, and whether the parameter is fixed or free in the fit of this paper.

## APPENDIX D: VALIDATION

As a simple validation test, the expected number counts output from *GalmodBD* for a field with unit solid angle, in the case of a uniform BD LF of  $n_0 \text{ pc}^{-3}$ , and towards the Galactic poles may be compared to the trivial analytical solution for this particular case, which comes from direct integration of the fundamental equation of stellar statistics for a single disc exponential model:

$$N(m) = n_0 [h_z f_1(d_1, d_2) + 2 h_z^2 f_2(d_1, d_2) + 2 h_z^3 f_3(d_1, d_2)] \quad (\text{D1})$$

In the expression above, if  $m, m + dm$  is some chosen bin in apparent magnitude,  $N(m)dm$  will be the number of objects in the given bin.  $h_z$  is the model exponential scale height for the disc, and

$$f_1(d_1, d_2) = d_1^2 \exp(-d_1/h_z) - d_2^2 \exp(-d_2/h_z) \quad (\text{D2})$$

$$f_2(d_1, d_2) = d_1 \exp(-d_1/h_z) - d_2 \exp(-d_2/h_z) \quad (\text{D3})$$

$$f_3(d_1, d_2) = \exp(-d_1/h_z) - \exp(-d_2/h_z), \quad (\text{D4})$$

where

$$d_1 = 10^{(0.2(m - M_{fi} + 5))} \text{ pc} \quad (\text{D5})$$

$$d_2 = 10^{(0.2(m - M_{br} + 5))} \text{ pc} \quad (\text{D6})$$

are, respectively, the minimum and maximum distances out to which any BD can be observed with the apparent magnitude  $m$ . This minimum (maximum) distance inevitably corresponds to the least (most) luminous BD spectral type in some filter, whose absolute magnitude is  $M_{fi}$  ( $M_{br}$ ).

Another simple validation test, again for the same special case as before, but this time involving all spectral types, is provided by the cumulative counts within some magnitude range  $[m_{br}, m_{fi}]$ ,  $N(\leq m)$ :

$$N(\leq m) = \sum_k^{N_{\text{mod}}} n_0 [h_z f_1(k, d_1, d_2) + 2 h_z^2 f_2(k, d_1, d_2) + 2 h_z^3 f_3(k, d_1, d_2)], \quad (\text{D7})$$

where in the expression above, the sum is over all  $N_{\text{mod}}$  BD spectral types, and the functions  $f_1$ ,  $f_2$ , and  $f_3$  are as given before. The minimum and maximum distances are now given by

$$d_1 = 10^{(0.2(m_{br} - M_k + 5))} \text{ pc} \quad (\text{D8})$$

$$d_2 = 10^{(0.2(m_{fi} - M_k + 5))} \text{ pc} \quad (\text{D9})$$

therefore corresponding to the minimum and maximum distances over which the  $k$ -th model contributes to the counts.

Completely analogous analytic expressions apply to the situation in which we model the number counts for  $(l, b) = (180, 0)$  deg. In



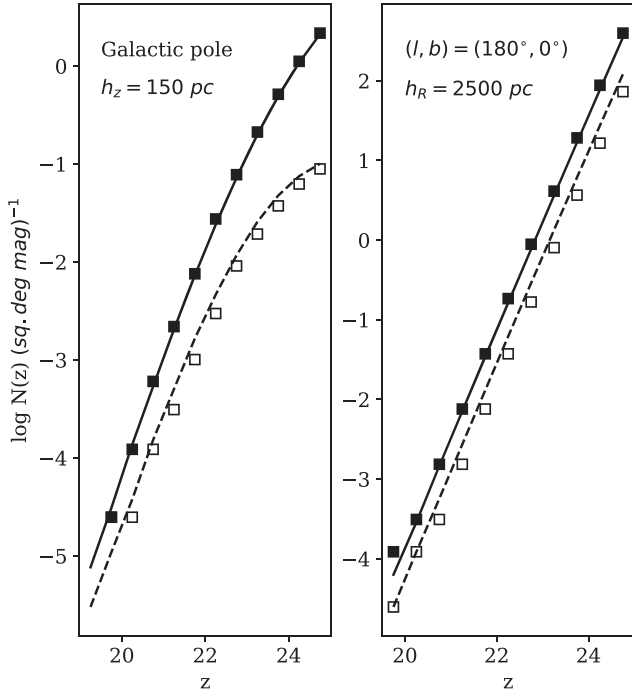


**Figure D1.** Left-hand panel: Star counts as a function of  $z_{AB}$  towards the Galactic Pole using a single disc model with scale height  $h_z^{\text{thin}} = 150$  pc. Points come from *GalmodBD*: the open symbols are differential counts and the filled symbols are cumulative counts. The associated curves are the analytic formulae given by equations (D1) and (D7), respectively. Right-hand panel: Same as in the previous panel, but now star counts towards the Galactic anticentre, for a model with a single disc with horizontal scale length  $h_R^{\text{thin}} = 2.5$  kpc.

this case, all one needs to do is to replace the model disc scale height  $h_{z,\text{thin}}$  by the scale length  $h_R$ .

In Fig. D1, we show the comparison of *GalmodBD* predictions with the analytical counts, based on a single disc component over a  $1 \text{ deg}^2$  field, and using  $n_0 = 4 \times 10^{-4} \text{ pc}^{-3} \text{ mag}^{-1}$ , for the following cases: 1 – Galactic pole (left-hand panel, using  $h_z^{\text{thin}} = 150$  pc); 2 –  $(l, b) = (180, 0)$  deg (right-hand panel, with  $h_R^{\text{thin}} = 2500$  pc). The points are from *GalmodBD* and the lines are from the analytic expressions provided above. Open (filled) symbols are differential (cumulative) counts as a function of  $z$ -band magnitude. *GalmodBD* clearly reproduces the expected counts.

<sup>1</sup>Centro de Investigaciones Energéticas, Medioambientales y Tecnológicas (CIEMAT), Av. Complutense, 40, 28040, Madrid, Spain

<sup>2</sup>Laboratório Interinstitucional de e-Astronomia – LIneA, Rua Gal. José Cristino 77, Rio de Janeiro, RJ 20921-400, Brazil

<sup>3</sup>Observatório Nacional, Rua Gal. José Cristino 77, Rio de Janeiro, RJ 20921-400, Brazil

<sup>4</sup>Instituto de Física, UFRGS, Caixa Postal 15051, Porto Alegre, RS 91501-970, Brazil

<sup>5</sup>Center for Astrophysics Research, University of Hertfordshire, Hatfield AL10 9AB, UK

<sup>6</sup>Harvard-Smithsonian Center for Astrophysics, Cambridge, MA 02138, USA

<sup>7</sup>Black Hole Initiative at Harvard University, 20 Garden Street, Cambridge, MA 02138, USA

<sup>8</sup>George P. and Cynthia Woods Mitchell Institute for Fundamental Physics and Astronomy, and Department of Physics and Astronomy, Texas A&M University, College Station, TX 77843, USA

<sup>9</sup>Institute of Astronomy, University of Cambridge, Madingley Road, Cambridge CB3 0HA, UK

<sup>10</sup>Kavli Institute for Cosmology, University of Cambridge, Madingley Road, Cambridge CB3 0HA, UK

<sup>11</sup>Physics Department, 2320 Chamberlin Hall, University of Wisconsin-Madison, 1150 University Avenue, Madison, WI 53706-1390, USA

<sup>12</sup>LSST, 933 North Cherry Avenue, Tucson, AZ 85721, USA

<sup>13</sup>Fermi National Accelerator Laboratory, PO Box 500, Batavia, IL 60510, USA

<sup>14</sup>Kavli Institute for Cosmological Physics, University of Chicago, Chicago, IL 60637, USA

<sup>15</sup>Instituto de Física Teórica UAM/CSIC, Universidad Autónoma de Madrid, E-28049 Madrid, Spain

<sup>16</sup>Cerro Tololo Inter-American Observatory, National Optical Astronomy Observatory, Casilla 603, La Serena, Chile

<sup>17</sup>Department of Physics and Astronomy, University of Pennsylvania, Philadelphia, PA 19104, USA

<sup>18</sup>Department of Physics & Astronomy, University College London, Gower Street, London WC1E 6BT, UK

<sup>19</sup>Kavli Institute for Particle Astrophysics & Cosmology, PO Box 2450, Stanford University, Stanford, CA 94305, USA

<sup>20</sup>SLAC National Accelerator Laboratory, Menlo Park, CA 94025, USA

<sup>21</sup>Department of Astronomy, University of Illinois at Urbana-Champaign, 1002 W. Green Street, Urbana, IL 61801, USA

<sup>22</sup>National Center for Supercomputing Applications, 1205 West Clark St., Urbana, IL 61801, USA

<sup>23</sup>Institut de Física d'Altes Energies (IFAE), The Barcelona Institute of Science and Technology, Campus UAB, E-08193 Bellaterra (Barcelona), Spain

<sup>24</sup>Institut d'Estudis Espacials de Catalunya (IEEC), E-08034 Barcelona, Spain

<sup>25</sup>Institute of Space Sciences (ICE, CSIC), Campus UAB, Carrer de Can Magrans, s/n, E-08193 Barcelona, Spain

<sup>26</sup>Santa Cruz Institute for Particle Physics, Santa Cruz, CA 95064, USA

<sup>27</sup>Institució Catalana de Recerca i Estudis Avançats, E-08010 Barcelona, Spain

<sup>28</sup>Department of Astrophysical Sciences, Princeton University, Peyton Hall, Princeton, NJ 08544, USA

<sup>29</sup>School of Physics and Astronomy, University of Southampton, Southampton SO17 1BJ, UK

<sup>30</sup>Instituto de Física Gleb Wataghin, Universidade Estadual de Campinas, 13083-859 Campinas, SP, Brazil

<sup>31</sup>Physics Department, Brandeis University, 415 South Street, Waltham, MA 02453, USA

<sup>32</sup>Computer Science and Mathematics Division, Oak Ridge National Laboratory, Oak Ridge, TN 37831, USA

<sup>33</sup>Department of Physics, University of Michigan, Ann Arbor, MI 48109, USA

<sup>34</sup>Argonne National Laboratory, 9700 South Cass Avenue, Lemont, IL 60439, USA

This paper has been typeset from a  $\text{\TeX}/\text{\LaTeX}$  file prepared by the author.